REPORT DOCUMENTATION PAGE	Form Approved OMB No. 0704-0188

The public reporting burden for this collection of information is estimated to average 1 hour per response, including the time for reviewing instructions, searching existing data sources, gathering and maintaining the data needed, and completing and reviewing the collection of information. Send comments regarding this burden estimate or any other aspect of this collection of information, including suggestions for reducing the burden, to Department of Defense, Washington Headquarters Services, Directorate for Information Operations and Reports (0704 0188), 1215 Jefferson Davis Highway, Suite 1204, Arlington, VA 22202-4302. Respondents should be aware that notwithstanding any other provision of law, no person shall be subject to any penalty for failing to comply with a collection of information if it does not display a currently valid OMB control number.
PLEASE DO NOT RETURN YOUR FORM TO THE ABOVE ADDRESS.

1. REPORT DATE *(DD-MM-YYYY)* 01/04/2012	2. REPORT TYPE FINAL	3. DATES COVERED *(From To)* 2008-2012

4. TITLE AND SUBTITLE		
Modeling Spin Testing Using Location Specific Material Properties	5a. CONTRACT NUMBER	FA9550-10-C-0056
	5b. GRANT NUMBER	
	5c. PROGRAM ELEMENT NUMBER	000102AB

6. AUTHOR(S)	
Alexander R. Bandar*, Ravi Shankar*, Wei-Tsu Wu*, Greg Olson**, Vikas Saraf***	5d. PROJECT NUMBER
* SFTC ** Northwestern University *** Ladish Corporation	5e. TASK NUMBER
	5f. WORK UNIT NUMBER

7. PERFORMING ORGANIZATION NAME(S) AND ADDRESS(ES)	8. PERFORMING ORGANIZATION REPORT NUMBER
Scientific Forming Technologies Corporation 2545 Farmers Drive, Columbus, OH 43235 and Northwestern University, Evanston, IL 60208	

9. SPONSORING/MONITORING AGENCY NAME(S) AND ADDRESS(ES)	10. SPONSOR/MONITOR'S ACRONYM(S)
Dr. Ali Sayir 875 North Randolph Street Suite 325, Room 3026, Arlington, Virginia 22203 Ali.Sayir@afosr.af.mil Phone: (703) 696-7236, Fax: (703) 696-7320	AFOSR
	11. SPONSOR/MONITOR'S REPORT NUMBER(S)

12. DISTRIBUTION/AVAILABILITY STATEMENT

DISTRIBUTION A. Approved for public release: distribution unlimited.

13. SUPPLEMENTARY NOTES

14. ABSTRACT

The work performed focused on incorporating modeling infrastructure into the finite element modeling code DEFORM to analyze disk behavior during spin pit tests using location specific material properties. The effects of residual stresses and local microstructure features from prior thermo-mechanical processing, along with centrifugal forces due to high cyclical rotational speed encountered during spin tests, were analyzed for their impact on permanent disk growth. Constitutive models for coupled grain evolution and precipitation were demonstrated, utilizing in-house models as well as models developed by Northwestern University, based upon the PrecipiCalc precipitation modeling software. Fully-coupled simulations between DEFORM and PrecipiCalc were performed, and evaluated by Ladish Corporation on an industrially relevant disk geometry and heat treatment schedule. Applicable flow stress prediction models were utilized. As a result of this work, DEFORM has been enhanced with improved microstructure prediction capabilities informed by physics-based precipitation codes, and virtual processing and testing models were evaluated by Ladish Corp.

15. SUBJECT TERMS

Spin pit testing, microstructural modeling, property prediction, finite element analysis, DEFORM, location specific material properties, burst speed

16. SECURITY CLASSIFICATION OF:			17. LIMITATION OF ABSTRACT	18. NUMBER OF PAGES	19a. NAME OF RESPONSIBLE PERSON
a. REPORT	b. ABSTRACT	c. THIS PAGE			
					19b. TELEPHONE NUMBER *(Include area code)*

Standard Form 298 (Rev. 8/98)
Prescribed by ANSI Std. Z39.18

Modeling Spin Testing Using Location Specific Material Properties

Final Report

Air Force STTR Contract FA9550-10-C-0056

Program Manager: Dr. Ali Sayir

Scientific Forming Technologies Corporation

Columbus, OH

2012

Modeling Spin Testing Using Location Specific Material Properties

Final Report

Air Force STTR Contract FA9550-10-C-0056

Program Manager: Dr. Ali Sayir

Scientific Forming Technologies Corporation

TABLE OF CONTENTS

LIST OF FIGURES

LIST OF TABLES

1.0 INTRODUCTION
Program Abstract

Jet engine disk components are increasingly subjected to higher operating temperatures. To meet the demands of increasing thrust and higher operating temperatures, a newer generation of nickel based superalloys such as LSHR, Alloy 10, Rene104 and RR1000 are being processed with dual microstructure distributions. Fine grain, high strength, fatigue resistant bore properties are contrasted with coarser grain, creep resistant rim properties. In order to optimize bore and rim properties of the engine disk, innovative dual microstructure heat treatment methods (DMHT) are employed where the bore is heated and cooled from sub-solvus temperature while the rim is heated and cooled from super-solvus temperature. The reliability of jet engine disks processed via DMHT method are evaluated by traditional spin testing where the disk is subjected to cyclical loading. Of particular interest is the transition zone between the bore and rim of the disk.

The current work focused on developing and enhancing the DEFORM system to model turbine disk spin testing as well as in-service performance with location specific material properties. Models developed during this program have the ability to consider location specific bulk residual stresses and microstructure features induced from prior manufacturing processes. The effects of thermal loading, cyclic loading, gravity, centrifugal forces, creep, and precipitation coarsening have been coupled to predict the evolution of residual stresses, resulting distortion and microstructure evolution as necessary. In this project, strength and creep models that can link the evolution of microstructural features to property response during thermo-mechanical processing as well as spin test and service conditions have been developed and implemented.

Anticipated benefits

Currently, there is no modeling system available to the industry which takes location specific material properties including microstructural features into consideration in predicting disk behavior during spin test. The industry lacks a modeling system that is capable of predicting mechanical property response such as strength, creep, flow stress and fatigue resistance due to prior thermo-mechanical processing, accompanying microstructural changes and exposure to service conditions.

The work developed during this program addresses the short comings of the current capability and the needs of the industry in modeling spin tests. This program demonstrated that the DEFORM system, with the newly implemented analytical models, can take into account the thermal transients and the cyclical loading conditions in the disk during spin testing to analyze the effects of grain size and precipitate size on plastic strain, tensile strength and residual stress redistribution.

As a result of this work, jet engine OEMs will be able to have a better understanding of the interaction of microstructural features and disk behavior under service conditions. The modeling infrastructure and methodology developed in this program will serve as a

solid platform to develop microstructure and property prediction models during thermo-mechanical processing and performance under service conditions for a variety of alloy systems, processes, components and industries.

Significance of the opportunity

Modeling material behavior during spin pit test results in the following benefits to the jet engine manufacturers:
e

- capability to include location specific material properties, residual stresses and microstructural features from prior processing in modeling spin test

- improved understanding of interaction of microstructural features on mechanical property response such as strength under service conditions

- ability to predict "hot spots" i.e., permanent growth of a disk component and evolution of residual stresses during spin testing and service

- ability to understand and optimize the processing window during the thermo-mechanical processing of jet engine components, specifically DMHT process, to push the existing limits of jet engine performance in service.

1.1   Background to turbine disk spin pit testing

Spin pit testing involves destructive or non-destructive testing of turbine disks at elevated temperature. The disk is rotated to service speeds, and evaluated for post-test non-recoverable distortion as well as burst speed. The test may be performed for a short time or for a full mission cycle (hours).

As most of the load of the centrifugal forces of the rotating disk is acting on the center of the disk (the bore), it is critical that this portion of the disk have high strength. A fine grained microstructure is typically preferred for enhanced strength properties. As the rim of the disk may experience higher operating temperatures, it is critical that this portion of the disk have high creep resistance. A coarse grain microstructure is typically preferred for improved creep resistance. The Dual Microstructure Heat Treatment (DMHT) process can produce this type of graded microstructure throughout a single component.

1.2   Dual Microstructure Heat Treatment (DMHT): motivation for
        location-specific property modeling

The DMHT process involves heating an as-forged turbine disk to supersolvus temperatures, and then selectively cooling different surfaces at different rates, in order to maintain a distribution of temperatures from the rim to the bore (Figure 1). By

maintaining the rim temperature supersolvus, gamma prime precipitates remain dissolved in the gamma matrix, and thus are not present to impede grain growth. The microstructure in this region thus coarsens to a large-grained microstructure, which is preferred for good creep properties. By maintaining the bore at a subsolvus temperature, gamma prime primary, secondary, and tertiary particles precipitate out of the solution; their presence retards grain growth by the phenomenon of Zener pinning, and the microstructure in this region remains fine-grained, which is ideal for good strength. The region between the supersolvus rim and subsolvus bore is referred to as the "transition zone", and results in an imperfect mix of large and small grains, a gradient in precipitates, and represents a microstructural feature in the disk which results in difficult-to-predict performance properties. Thus the need for computer simulation of the DMHT process, prediction of the local microstructure, extrapolation of the local microstructure to local properties, and ultimately to estimation of the performance of the macroscopic disk during spin tests or in service.
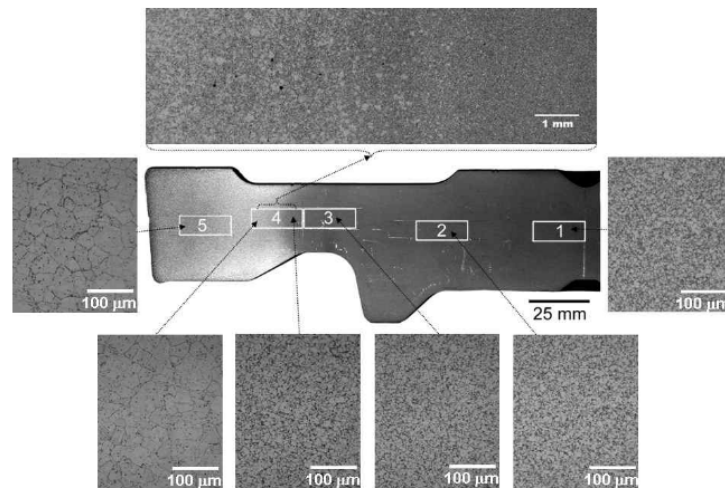
Figure 1. LSHR DMHT Microstructure in the transition zone[1].

1.3   Theory of microstructure evolution modeling

Historically, correlation between process conditions and observed microstructure has been possible in a largely empirical sense. A coupon can be held at elevated time and temperature, and the resulting grain growth can be plotted as a function of time, temperature, initial grain size, etc. Equally, a coupon can be forged to various strains at different temperatures and strain rates, and the resultant grain refinement can be plotted as a look-up-table or can be fitted to empirical equations such as the Johnson-Mehl-Avrami-Kolmogorov (JMAK) equation. The evolution of microstructure can thus be roughly correlated to process parameters such as ram speed, preheat temperature, heat treatment conditions, etc.

Recently, more sophisticated models which bring more of the physical phenomena into the equations have been developed, and incorporated into Finite Element Modeling (FEM) packages such as the commercial code DEFORM. Thus, an initial workpiece

geometry may be defined; a process condition may be specified (furnace soak; deformation; forging; service test; etc); the process parameters (e.g. furnace temperature; ram speed) induce a gradient of state variables throughout the discretized workpiece mesh; and these state variables influence the evolution of local microstructure. This local microstructure, in turn, influences the local workpiece microstructure, which in turn goes back to influence the response of state variables (e.g. strain, strain rate) to the next iteration of process conditions.

The next few sections detail a few of the physical phenomena wherein processing conditions influence the microstructure.

1.3.1 Recrystallization

Recrystallization is the phenomenon which describes how new, fine grains can nucleate and grow out of a deformed microstructure during deformation (which is called "dynamic recrystallization", or DRX); or in which these new, fine grains nucleate and grow out of a post-deformation workpiece, either immediately after deformation ("metadynamic recrystallization", or MRX) or some time after deformation ("static recrystallization", or SRX). This phenomenon produces a fine grained microstructure, which is good for enhanced strength properties.

1.3.2 Grain growth

While at elevated temperature, grain boundary mobilities increase, making it easier for them to migrate. As grain boundaries represent an additional source of energy in the microstructure (a mismatch of the atomic lattice at the grain interfaces), and since all systems thermodynamically strive to reduce their energy, grain boundaries migrate in such a way as to minimize their surface area, which results in an effective "growth" of the grains. Thus, when at elevated temperature for extended periods of time, the average grain diameter of a microstructure will grow.

DEFORM's previous grain growth model was largely empirical - an exponential function long-tested in the literature, which is a conventional way to correlate grain growth to initial grain size, time, and temperature. However, it does not take into account grain boundary curvature, and hence the reduced grain boundary migration velocity as a grain grows. For short periods of time (for example, rapid furnace heating, or transfer from a furnace to a die, or during rapid deformation) this equation is sufficient to predict grain growth (Figure 2, left). However, at prolonged periods (greater than ~30 minutes for nickel base alloys at solution temperature) this equation over-predicts grain size; grains simply continue to grow, even though an equilibrium grain size should eventually be reached, as a function of temperature (Figure 2, center). However, if grains exist in a matrix of pinning precipitates, then grain growth is impeded regardless of the time (Figure 2, right).
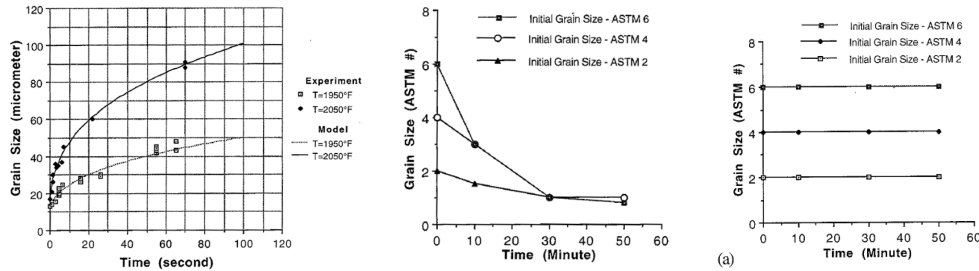
Figure 2. Left - exponential growth of grains, at high temperature and short time. Center - saturation of grain growth, unimpeded by precipitates (1121°C). Right - growth impeded by pinning precipitates (1010°C)[2].

During this project, the grain growth algorithm was enhanced to include grain boundary migration velocity as a function of instantaneous local grain size; this results in both a slowing of the grain boundary migration velocity as a function of coarsening grain size, as well as a saturation of grain size as a function of temperature - two phenomena which occur in nature (as depicted in Figure 2), but only as a result of this project are now predicted appropriately in DEFORM.

1.3.3 Precipitation

The presence of alloying elements in a material can dissolve or precipitate out of the matrix, depending on the thermodynamic stability of the resulting material crystal structure at any given time and temperature. At subsolvus temperatures, the crystal structure of the gamma prime constituent phase of LSHR, for example, is thermodynamically more stable than the same composition of elements dissolved into the matrix. Thus, precipitates are present below the solvus temperature. At supersolvus temperatures, the gamma matrix can thermodynamically support a dissolved composition of the constituent elements of the gamma prime phase more easily than the gamma prime precipitate phase - and thus the precipitates dissolve into the matrix.

The conventional method that this phase transformation is predicted has been from empirical look-up-tables such as Time-Temperature-Transformation (TTT) tables, or from constitutive equations which predict volume fractions of a certain phase as function of the local state variables (time, temperature, elemental composition, stress state, etc). These are the previous methods with which DEFORM would predict volume fractions of secondary phases. However, volume fraction alone is a very coarse definition of the state of a second phase. In reality, the second phase emerges as a field of individual particles - and thus, to more fully describe the manifestation of a second phase as the disk cools below the solvus temperature, it is necessary to know either the size of the particles or the number density of the particles. Total volume fraction of a second phase is naturally the volume of each individual particle multiplied by the number density of the particle; thus, if one knows 2 of these 3 variables, one can describe the general presence of the second phase in the matrix. (This assumes that all particles are adequately described by the average particle size, and assumes that they are uniformly distributed throughout the matrix. More advanced models predict the distribution of precipitate sizes, as well as the

topology of the phases within the microstructure - such as whether they are located on grain boundaries, on other second phases, or within the bulk of the matrix grains).

During this project, the infrastructure with which DEFORM documents the presence of second phases locally throughout a workpiece was enhanced to *also* include the precipitate sizes. This is important not only for improved microstructural representation, but it also allows finer structure-property equations. When a second phase comprises the bulk of a material (for example, ferrite, bainite, martensite phases in steels) the properties may roughly be derived as a "rule of mixtures" of the constituent phases. However, when precipitate volume fractions are much smaller (i.e. a few percent) this rule of mixtures algorithm breaks down, and more physics-based structure-property laws (such as the Zener pinning phenomenon) need as input more specific microstructure feature descriptions - such as size and number density.

1.3.4 Zener pinning

Grain boundaries experience a retarding force when they migrate past a particle; the traversal of the grain boundary across a precipitate creates a new interface, which adds more energy to the system, and thus represents a thermodynamic obstacle[8]. In this manner, precipitates slow or stop grain boundary growth; this phenomenon is referred to as Zener pinning. Microstructures populated with a distribution of precipitates thereby maintain finer average grain sizes than equivalent microstructures maintained at the same time and temperature which do not contain particles.

During this program, DEFORM's equations which predict grain growth have been enhanced to include the Zener pinning phenomenon. In this way, DEFORM can more accurately predict the effect of the local presence or absence of particles (as is produced during the DMHT process) on the resultant grain size. Examples will follow in later sections.

1.4   Theory of property prediction
1.4.1 Flow stress

The mechanism for deformation of most metals is the motion of dislocations through the crystalline lattice. As such, the flow stress of a material can often be decomposed into various contributions from different aspects of the microstructure that affect dislocation motion. As a material deforms, dislocations move and leave tracks throughout the crystal - these tracks represent obstacles for other dislocations, and thus the more a material deforms, the harder it becomes to continue deforming the material - this is the phenomenon of strain hardening or work hardening. In addition to tracks left by previous dislocations, grain boundaries are also an obstacle to dislocation motion. Since finer grains mean more grain boundaries, a fine-grained microstructure leads to a shorter mean-free-path for dislocations to move before they collide with and stop at a grain boundary - resulting in a stronger microstructure. This is the Hall-Petch phenomenon. The presence of fine precipitates not only pin grain boundaries, keeping the

microstructure fine-grained, but they also act to impede dislocation motion, leading to the phenomenon of precipitation hardening. The presence of solute atoms dissolved in the matrix phase serves to elastically deform the lattice, making it more difficult for dislocations to glide through the material, giving rise to the phenomenon of solute strengthening. By performing the appropriate "microstructural bookkeeping" of each of these microstructural features, and providing them as inputs to a correlated strength model, the local contribution of the local microstructure features to the local strength may be deduced, and ultimately used to predict the macroscopic performance of the component.

During this project, DEFORM has enhanced its strength property prediction model with such a correlative equation, relating local microstructure features (as evolved by prior processes) to the local flow stress.

1.4.2 Creep

At elevated temperatures and under a constant applied load, materials may deform very slowly - this is referred to as "creep". The mechanism for this deformation is typically sliding of grains past each other (grain boundary sliding). In contrast to flow stress, the *larger* the grains, the better the creep resistance, since there are fewer grain boundaries to accommodate grain boundary sliding.

During this project, DEFORM's creep model algorithm was enhanced to take into account the local grain size; in this way, creep is now a local function of the microstructure, and the creep behavior of DMHT disks during testing or in service may be more accurately predicted.

1.4.3 Integrated flow stress model

Northwestern University provided a flow stress model derived from Tresa Pollock's5 work. This includes a component of strength due to solid solution strengthening, which is influenced by temperature; a component of strength due to grain size; a component of strength due to shearing/bowing of secondary gamma prime strong pair coupling; a component of strength due to shearing/bowing of tertiary gamma prime strong pair coupling; and a component of strength due to cross-slip induced strengthening from the gamma prime phase.

1.4.4 Bauschinger Effect

During cyclic loading, the response of the flow stress to applied stress is influenced by the prior deformation. This is particularly important during turbine disk spinning, since the ramp-up and ramp-down of the rotation of the disk represents a single cycle - and aviation turbine disks experience thousands of such cycles during their lifetime.

During this project, the ability to model the Bauschinger effect was enhanced in DEFORM; more details will be discussed in the results section.

2.0 DISCUSSION OF RESULTS

The thermal and mechanical properties of LSHR are available in the LSHR NASA report[3]. A generic aviation turbine disk geometry was used for the DMHT simulation, machining, and spin pit testing. The as-forged and as-machined geometries are presented below.
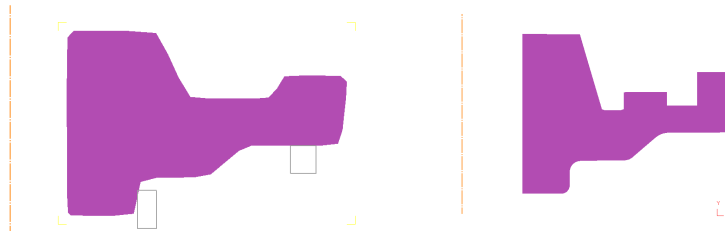

Figure 3. Left - as forged disk geometry. Right - as machined disk geometry.

2.1   Process

The as-forged geometry was initialized with a uniform grain size of 4 microns across the entire disk. This was assumed based upon micrograph data available in the LSHR NASA report[3].

The disk was then exposed to a heat-up; a DMHT process; a cool down; multiple machining steps; and then a spin test. The simulation was "rigid-plastic" for the heat-up and for the DMHT processes. The simulation was "elasto-plastic" for the cool down, machining, and spin testing - this way, it is possible to capture the residual stress distribution induced by cooling; the distortion caused by material removal; and the effect of an initial residual stress distribution on the performance (yielding, distortion) during spin testing. All of the microstructural variables (grain size, precipitate size, precipitate volume fraction) were evolved and carried through from simulation to simulation.

2.1.1 Solutionizing

The figures below depict an example solutionizing process, in which the as-forged disk is inserted into a furnace for a prescribed time and temperature. Three points are tracked for their state variable history; Figure 4 shows the temperature distribution. Figure 5 plots the temperature at the rim, transition zone, and bore. Figure 6 presents resultant grain size distributions as a function of the underlying temperature contours. Figure 7 plots the grain sizes at the rim, transition zone, and bore.

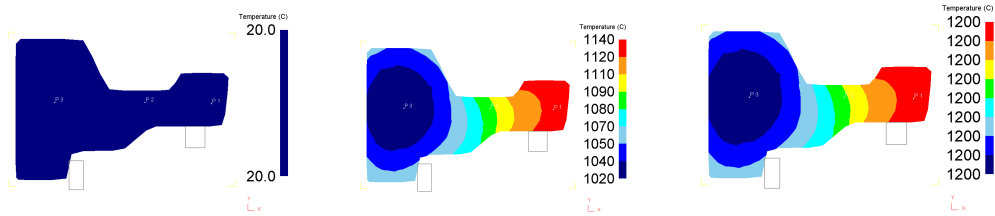Figure 4. Temperature profile in the as-forged disk during heating, at start, mid-process, and end of solutionizing.
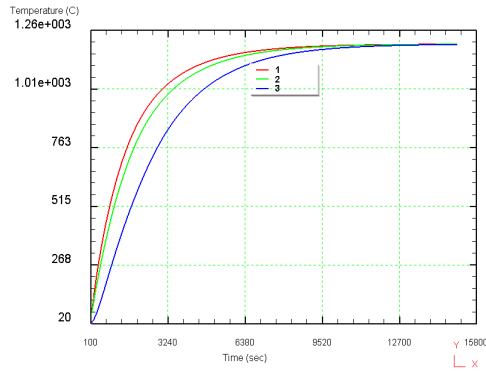

Figure 5. Plots of temperature at three different locations (rim, transition zone, and bore).
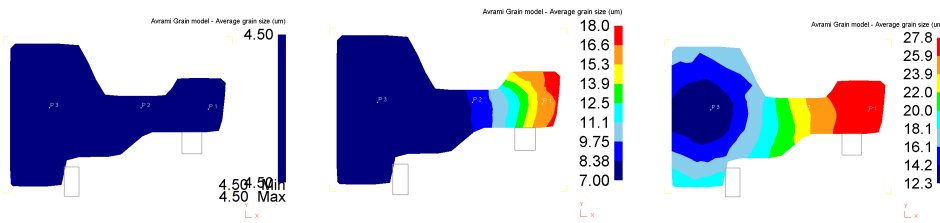

Figure 6.   Grain size contours of the as-forged disk at the beginning, mid-process, and end of solutionizing.
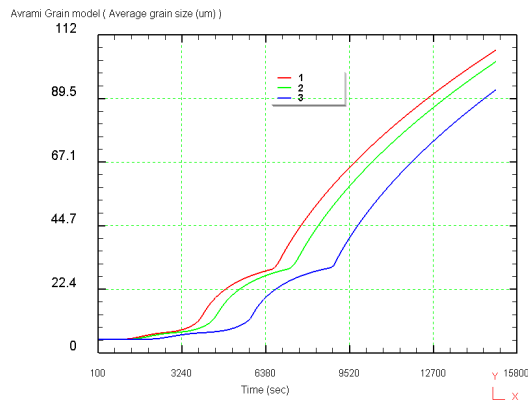

Figure 7. Plots of grain size at 3 different locations during heating (rim, transition zone, and bore).

Note that Figure 7 depicts grain growth beginning sluggishly at low temperature and with a full field of pinning precipitates; as temperature rises and exceeds the gamma prime secondary solvus, these precipitates dissolve and grain growth accelerates, then plateaus as the grain boundary curvature flattens with grain coarsening. As the temperature continues to rise and exceeds the gamma prime primary solvus, the last remaining precipitates to pin the grain boundaries dissolve and grain growth accelerates again, and approaches another flattening as the new saturated grain boundary curvature limit is approached. Note, too, that this solutionizing simulation was run to a much longer time than would be industrially relevant, in order to demonstrate the behavior of the grain growth and precipitate pinning kinetics.
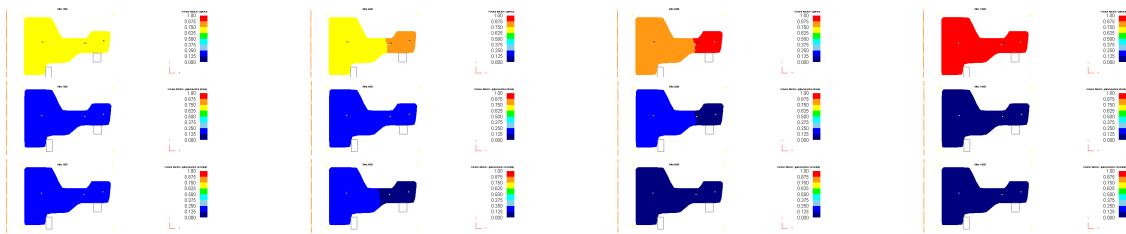
Figure 8. "Absolute" contour plots (from 0 to 1) of gamma phase volume fraction (top), gamma primary phase (middle), and gamma secondary phase (lower), during beginning (left figure), middle (center figures), and end (right figure) of the solutionizing process.

Note that the rim region, which heats fastest due to its higher surface area to volume ratio, begins to dissolve gamma prime primary and secondary sooner than the bulk of the disk.
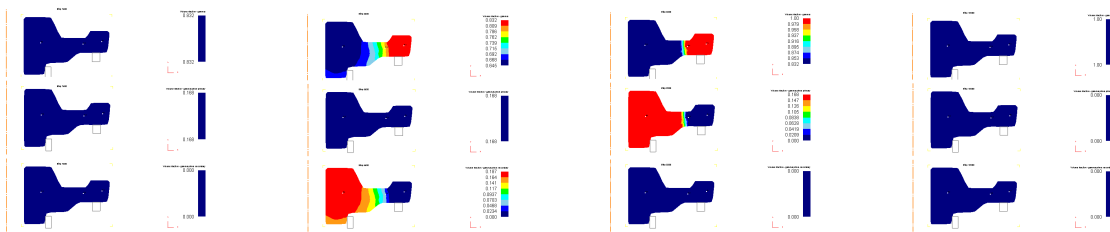
Figure 9. "Local" contour plots (from minimum to maximum volume fraction at each time step) of gamma phase volume fraction (top), gamma primary phase (middle) and gamma secondary phase (lower) during the beginning (left figure), middle (center figures), and end (right figure) of the solutionizing process.

Figure 9 displays the "locally scaled" contour plot feature in the DEFORM post processor, which provides finer resolution of the contours of the precipitate volume fractions than the "global" scale in Figure 8.

Figures 10-12 plot the point-tracked volume fractions of overall gamma prime volume fraction at the rim, transition zone, and bore (Figure 10) as well as the primary and secondary volume fractions (Figures 11, 12).

13
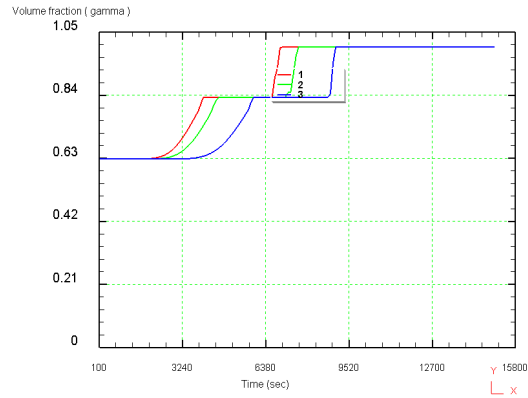
Figure 10. Volume fraction of gamma phase at three different points tracked on the as-forged disk; at the rim, the transition zone, and the bore.

Figure 11. Volume fraction of gamma prime primary phase at three different points tracked on the as-forged disk; at the rim, the transition zone, and the bore.

Figure 12. Volume fraction of gamma prime secondary phase at three different points tracked on the as-forged disk; at the rim, the transition zone, and the bore.

14

2.1.2 Dual Microstructure Heat Treatment

After solutionizing, the as-forged disk can be exposed to a variety of cooling processes. Below is an example of the DMHT process, wherein the rim is exposed to a slower cooling rate (effectively a higher temperature)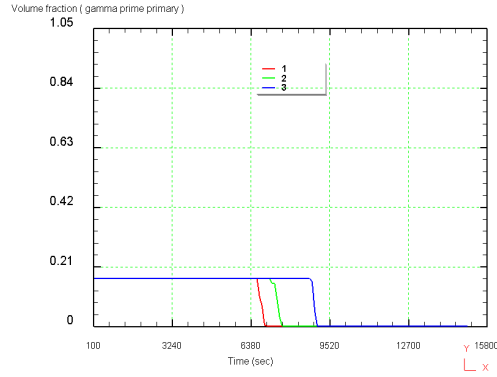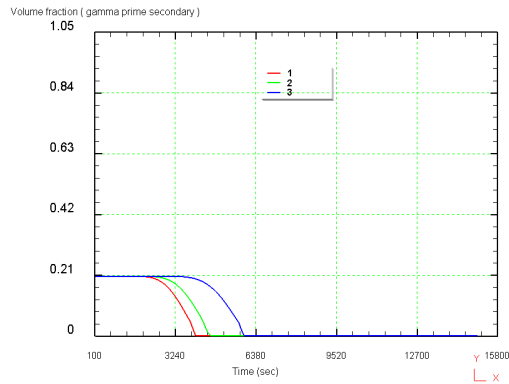 than the bore, resulting in a gradient in temperature above the solvus at the rim and below the solvus at the bore, which tailors the microstructure across the disk for an optimum combination of strength and creep resistance. Figure 13 depicts the temperature contours, and Figure 14 depicts the resultant grain size contours.
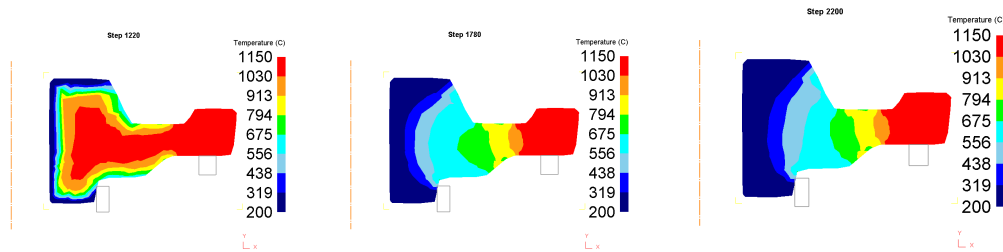
Figure 13. Temperature contours throughout the as-forged disk during the DMHT process, at start (left), mid-process (center) and end of process (right).
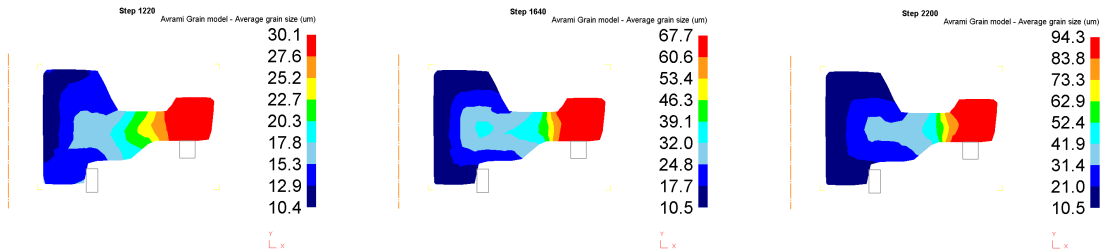
Figure 14. Grain size contours throughout the as-forged disk during the DMHT process, at start (left), mid-process (center) and end of process (right).

Note that in this example process, the grain size across the disk has coarsened due to the prior heat-up process. A more industrially tailored heating profile would result in less grain growth than exhibited in this example simulation. Note too that as the rim remains supersolvus, an absence of pinning precipitates allows the grains to grow very large; whereas the cooler bore region keeps grain growth sluggish, and more importantly, at subsolvus temperature maintains a field of precipitates that keeps grain boundaries pinned. Thus, Figure 14 illustrates, very small changes to grain size in the bore while the rim region experiences fairly large grain growth. Figure 15 plots the volume fraction of gamma, gamma prime primary, and gamma prime secondary populations across the disk.
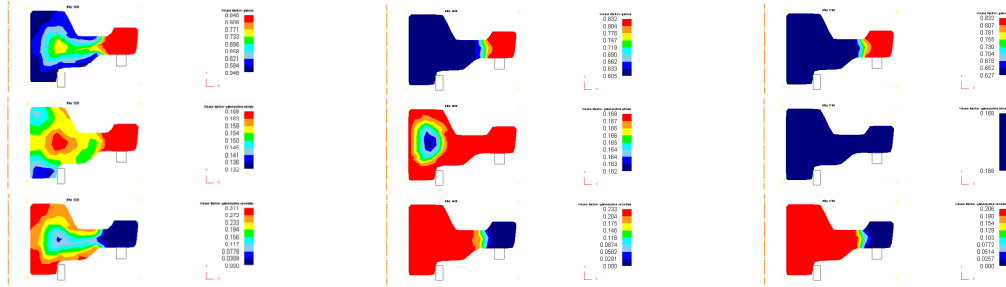
Figure 15. Contour plots of gamma (top), gamma prime primary (middle) and gamma prime secondary (bottom) during beginning (left), mid-process (center) and end (right) of DMHT process.

Note that as the rim remains at elevated temperature, above the gamma prime secondary solvus, the gamma prime secondary particles remain dissolved (bottom contour plots), yet are present in the cooler transition zone and bore of the disk.

The gamma prime primary precipitates, with a higher solvus temperature, are present more widely across the disk than the gamma prime secondary precipitates. However, as the disk maintains the DMHT temperature distribution they too more fully precipitate out across the disk.

2.1.3 Cooldown

During cooling, more of the precipitates come out of solution and populate the disk. Figure 16 presents the cooling temperature contours, and Figure 17a presents the average resulting grain sizes, as a result of coupled grain growth and precipitation.
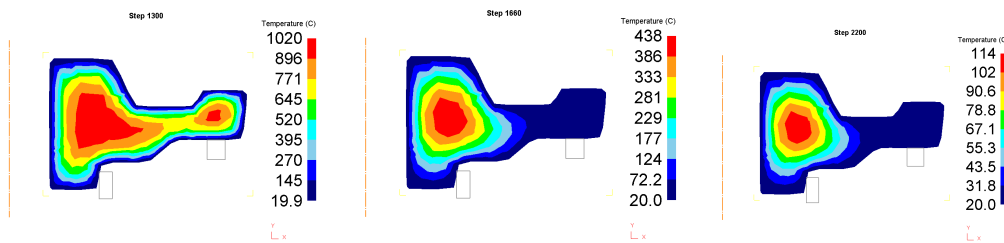
Figure 16. Temperature distribution during cool down from DMHT. Left - start of process; center - mid-process; right - end of process.
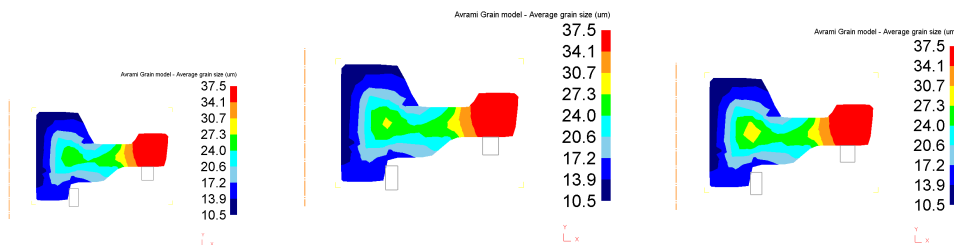
Figure 17a. Left - average grain size across disk before cooldown. Center - average grain size mid-cooldown. Right - average grain size post cooldown.

To simulate the grain evolution during cooldown, the grain size across the disk was initialized from a point in the DMHT process which achieved a grain size distribution similar to that evident in Figure 17b (disk macro) from the Gabb, Gayda, Kantzos, TMS, 2006. This is a distribution wherein the fine grain size at the bore is approximately 4.5 microns (ASTM grain size ~12.5) and the coarse grain size at the rim is approximately 34.5 microns (ASTM grain size ~7). The simulation results produced a grain size at the bore of approximately 10 microns (ASTM grain size ~10) and at the rim of approximately 37 microns (ASTM grain size 6.5). Note that this was without much tuning of the parameters, which includes thermal conductivity data, heat transfer data, grain growth kinetics, and more. Note that in Figure 17a, the bulk of the disk, which remains hotter than the faster cooling thinner section, does experience some grain growth.
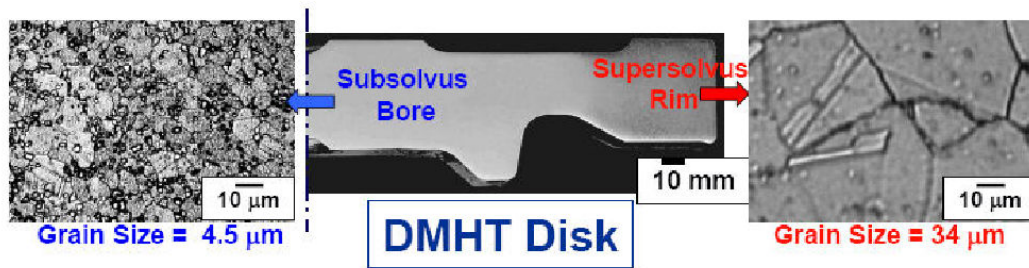
Figure 17b. Micrographs of grain size at bore and rim of DMHT disk.

Table 1. Comparison between grain sizes of bore and rim of DMHT disk from simulation and from literature.

	Bore	Rim
Simulation	10.5 microns	34.5 microns
Literature	4.5 microns	37.5 microns

The discrepancy in the bore grain size can be accommodated by better tuning the initial grain size post-forging (which was estimated) as well as by increasing the strength of Zener pinning to keep the grain sizes more refined in the presence of precipitates.

Figure 18 displays the volume fractions of gamma, gamma prime primary, and gamma prime secondary after cooling, as predicted by the "Fast Acting" model derived from PrecipiCalc, described later.
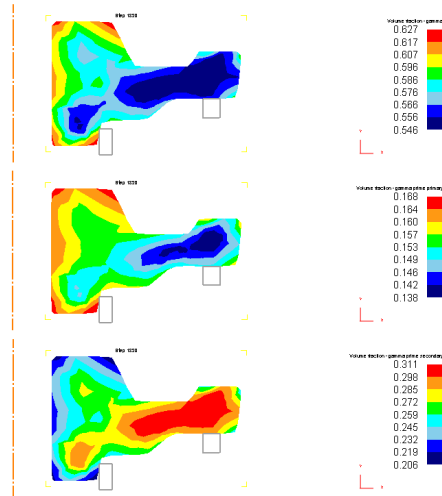
Figure 18. Volume fraction of gamma (top), gamma prime primary (middle) and gamma prime secondary (bottom) at end of cool down process, as calculated by the "Fast Acting" PrecipiCalc model.

Figure 19 displays the residual stress distribution during cool down; Figure 20 displays the elastic strain distribution throughout the disk during cooldown. Figure 21 displays the total displacement during cooling, as a result of elastic strain and thermal contraction.
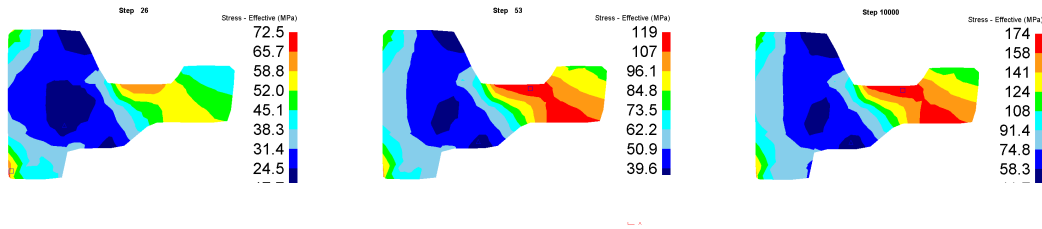
Figure 19. Residual stress distribution throughout the component during cool down (left - start of cool down; center - mid process; right - end of cool down).
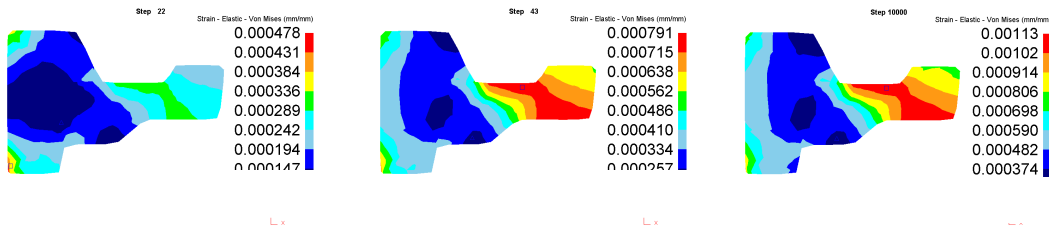
Figure 20. Elastic strain distribution throughout the component during cool down (left - start of cool down; center - mid process; right - end of cool down).
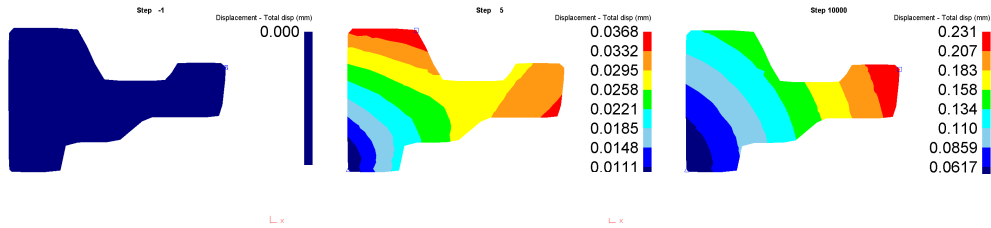
Figure 21. Total displacement distribution throughout the component during cool down
(left - start of cool down; center - mid process; right - end of cool down).

2.1.3.1 Coupling of PrecipiCalc and DEFORM

Precipitation may also be computed by coupling PrecipiCalc (a software developed by Questek that predicts precipitate size and volume fraction) through DEFORM. In the newest version of the DEFORM post-processor, enhanced during this project, the time-temperature profile of each element (or of a single point-tracked location) may be exported directly to PrecipiCalc, which is automatically spawned during this process. PrecipiCalc then performs a full computation of the phase transformation process, and sends the results back to DEFORM (volume fraction and size of precipitates). DEFORM then displays this data across the workpiece (Figure 22).
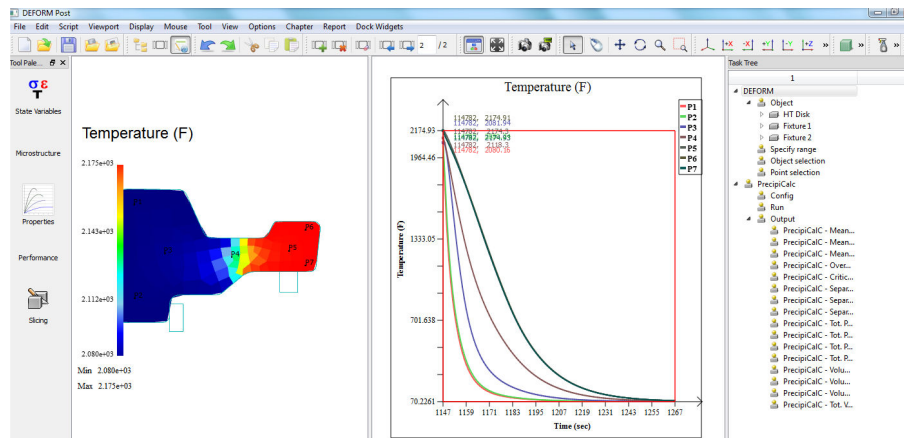
Figure 22. Exporting the time-temperature profiles of various locations in a DEFORM workpiece to PrecipiCalc.
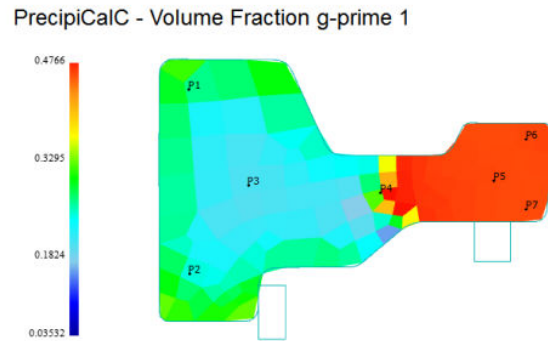
Figure 23. PrecipiCalc results of gamma prime primary volume fraction, displayed automatically in DEFORM.
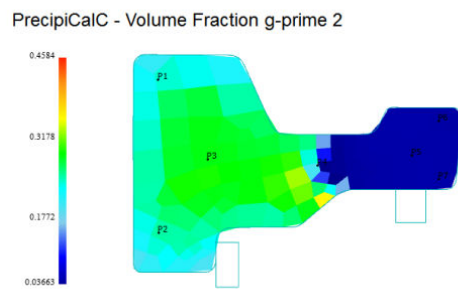
Figure 24. PrecipiCalc results of gamma prime secondary volume fraction, displayed automatically in DEFORM.
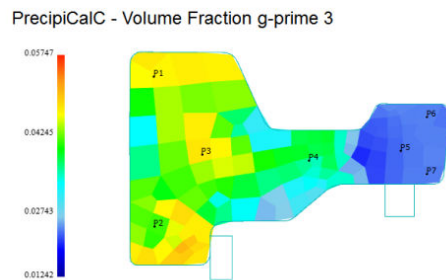
Figure 25. PrecipiCalc results of gamma prime tertiary volume fraction, displayed automatically in DEFORM.

(Note: Details of fast acting model is not discussed so far.. Should we not introduce fast acting model details here? Or refer to Page 25 for model details)

These results are compared to the "Fast Acting" results derived from PrecipiCalc, displayed in Figure 26.
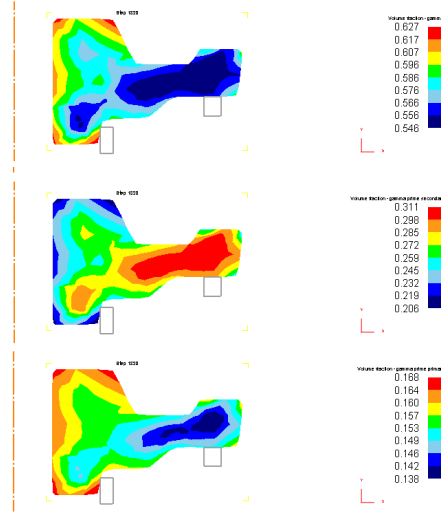
Figure 26. Top - gamma phase. Center - gamma prime primary phase. Bottom - gamma prime secondary phase.

2.1.4 Machining

The as-forged, heat treated, and cooled workpiece was then machined via a series of "boolean operations", in which material from the virtual workpiece is removed in
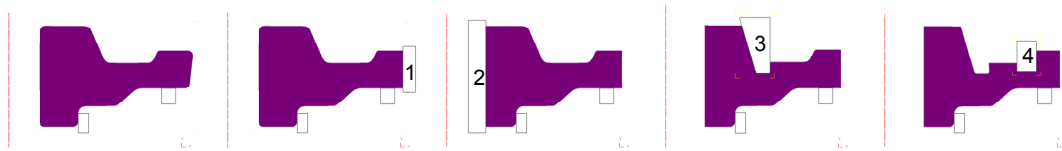
Figure 27. As-forged geometry, left; boolean machining passes 1-4 at right.

As material is removed in each boolean machining step, the residual stresses evolve and the part geometry distorts slightly. The evolution of the residual stresses and the distortion are captured in Figures 28 and 29.
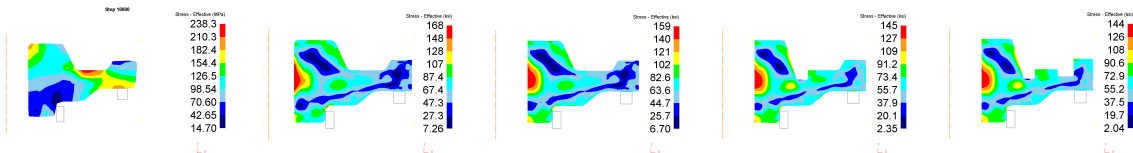
Figure 28. Evolution of residual stresses during boolean machining.
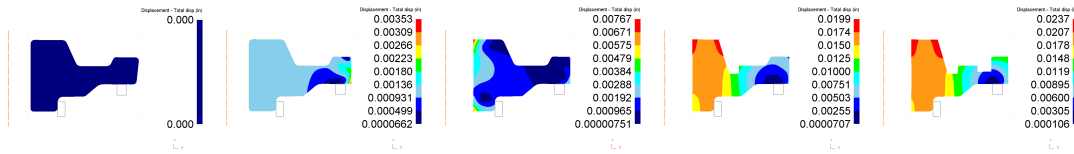
Figure 29. Evolution of distortion during boolean machining.

2.1.5 Spin test

Following the processes of heat up, DMHT, cool down, and boolean machining, the final part is now ready for spin pit test simulation. Figure 30 depicts the grain size, velocity, creep strain and total distortion accumulated at the start, mid portion, and end of a spin test.
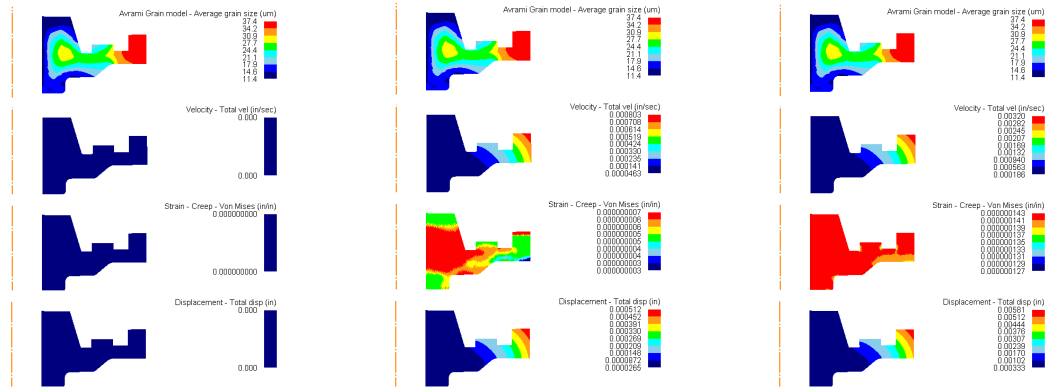
Figure 30. From top to bottom - grain size, velocity, creep strain, and total distortion. From left to right - start of spin test, mid portions of spin test, and end of spin test.
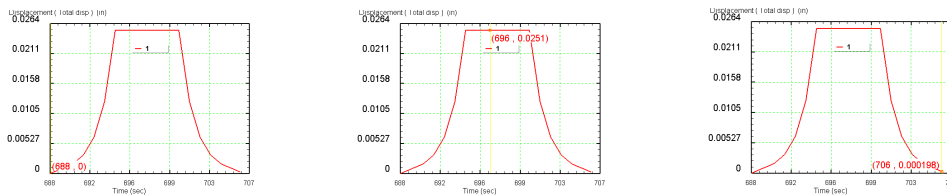
Figure 31. Displacement point-tracked at rim of disk.

Note that in Figure 30, the displacement across the disk was initialized to zero (clearing any displacement that may have accumulated during the prior processing steps). A point was tracked at the very top corner of the rim of the disk, and displacement graphed during a spin test. Figure 31 displays the distortion due to elastic and creep distortion; at the end of the spin test, the elastic distortion is recovered, and the displacement that

remains is due to creep. Creep strain rates are computed as a function of stress and underlying microstructure, as detailed below.

2.2 Microstructure Modeling
2.2.1 Grain size

Grain size is a function of initial cast grain structure, recrystallization during deformation, and growth during heating/annealing. The presence of precipitates can also impede grain growth and recrystallization.

DEFORM can predict grain size refinement during deformation via the recrystallization process. However, as this project is intended to capture the microstructure evolution, property prediction and performance analysis of a disk *after* deformation, from DMHT through machining through service testing, recrystallization is not modeled. Rather, the resultant grain size that was produced from hipped and extruded billet and disk forging is assumed, and taken to be the initial grain size provided to the DMHT simulation and subsequent processes. Micrographs of DMHT disks from the NASA report show that the finest grain sizes are ~4.5 microns. Since grains cannot get finer during DMHT - they may either remain the same size or get larger - the initial grain size prior to DMHT is assumed to be slightly finer, at ~4 microns. However, industrial application of this simulation process can either be informed by modeling the previous processing steps and carrying over the grain size, or it can be measured from as-forged disks prior to DMHT.
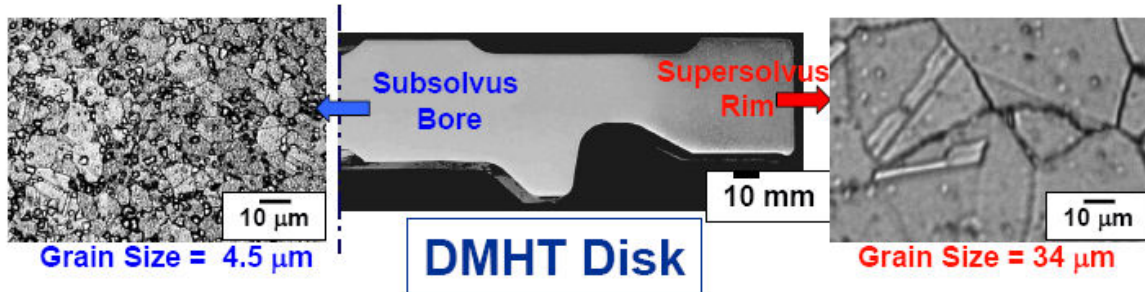
Figure 32. Micrographs of grain size at bore and rim of DMHT disk.

The previous grain size modeling equation in DEFORM is presented in Equation 1. This equation is empirical, and largely curve-fits the behavior of short-term grain growth to an exponential equation which is a function of time, temperature, initial grain size, and a few modeling constants. Thus, this equation predicts continued grain growth at elevated temperature, and neglects the driving force of grain boundary curvature and the retarding force of precipitates.

$$D = \left(D_0^m + at \exp\left(-Q/_{RT} \right) \right)^{1/m} \qquad Eq.\ 1$$

The enhanced grain size modeling equations implemented during this project are listed in Equations 2 and 3. Equation 2 predicts grain boundary migration velocity as a function of grain boundary curvature and the grain boundary surface energy. In this manner, a more physics-based approach to predicting grain growth is achieved; grains with higher curvature (given by the diameter, D) grow faster, but then as they grow large, their grain boundary curvature flattens, and the driving force to continue growing subsides. This results in the temperature-influenced grain growth saturation behavior observed in real materials.

$$v = M_0 \exp\left(-Q/RT\right)\left(3\frac{\gamma_s}{D}\right) \qquad \textit{Eq. 2}$$

Equation 3 depicts the interaction with local pinning precipitates. In this way, a counterpressure to grain growth exists when grain boundaries are navigating a field of precipitates. The finer the precipitates (defined by their diameter, d), and the greater their number (given by the volume fraction, Fv), the greater the retardation of grain boundary velocity, eventually leading to complete grain boundary pinning.

$$v = M_0 \exp\left(-Q/RT\right)\left(3\frac{\gamma_s}{D} - 3\frac{F_v \gamma_b}{d}\right) \qquad \textit{Eq. 3}$$

In this way, grain size and precipitate size and volume fraction may be coupled - this is especially critical in the DMHT process, wherein part of the disk is maintained supersolvus (absent precipitates) in order to encourage grain coarsening; whereas the rest of the disk is maintained subsolvus (to retain precipitates) and hence to maintain a fine grained structure. The enhancements implemented during this project can now predict this type of real physics-related behavior. (note: identify material constants and Mo, γ, Q, R etc)

2.2.2 Precipitation

Prior to this work, DEFORM predicted volume fractions of second phases via empirical models such as time-temperature-transformation (TTT) diagrams, the Magee equation for martensite, diffusion equations for other ferrous phases, etc. DEFORM did not however predict anything beyond the volume fraction of the phases present. In order to properly inform structure-property laws which require the diameter, number density, and even the shape of precipitates present, it is necessary to add more dimensions to the microstructural feature representation for precipitates. This was performed during this project by adding two new "key" words to DEFORM's database structure. This structure is the manner in which DEFORM performs the record keeping of state variables and microstructural features, among other things, and the two new words are "sizemode"

(SIZEMD) and "size-shape" (SIZESH). These allow DEFORM to know what type of precipitation algorithm to apply to different second phases that may emerge in a material, as well as how to record the size and/or shape of the precipitates as they nucleate, grow, coarsen, and dissolve.

The models for precipitation were provided by university partner Northwestern University, and represent "fast acting" versions of the precipitation software PrecipiCalc's algorithms for precipitation upon cooling.

Fast action model for computing primary and secondary γ' microstructure:

Required input information:
- Solution treatment temperature T_s (°C)
- Linear cooling rate, $\dot{T}$ (°C/sec) from T_s 25°C to 750°C, using regression. Note the linear cooling is a good assumption for the provided cooling profile for both interior and surface of TC1, TC3, and TC3 locations.

Fast action model for computing primary and secondary γ' microstructure
- Temperature dependent equilibrium γ' Phase fraction for LSHR, with a polynomial fit:

$$f_{\gamma'}^{eq}(T) = 0, \text{when } T > 1169.954\text{°}C \qquad \text{Eq. 4}$$

$f_{\gamma'}^{eq}$ = 1.6676982 + T(-0.0190091 + T (0.0001464666 + T (-6.5783205e-7 + T (1.8974787e-9 + T (-3.6667477e-12 + T (4.8054612e-15 + T (-4.2188928e-18 + T (2.3753241e-21 + T (-7.743258e-25 + T (1.1081783e-28)))))))))) $\qquad$ *Eq. 5*

- Primary γ' Microstructure at end of quenching:
  - Volume fraction (note, if result becomes negative, set it to zero)

$$f_1(T_S, \dot{T}) = f_{\gamma'}^{eq}(T_S) + 0.85276 - 0.02967 \log_{10}(\dot{T}) - 0.00071497\, T_S \qquad \text{Eq. 6}$$

  Within the range of T_s > 1130°C and < 1175°C and $\dot{T}$ > 0.7°C/s and < 12°C/s
  - Number density $N_1(T_S)$ (1/m³) is calculated with

$$\log_{10}(N_1(T_S)) = 16.7 + 0.20673(1170 - T_S)^{0.46827} \qquad \text{Eq. 7}$$

  - Mean particle radius R_1 (in meters), is described by

$$R_1 = 0.877 \left[\frac{f_1}{N_1 \frac{4\pi}{3}} \right]^{\frac{1}{3}} \qquad \text{Eq. 8}$$

  - The above equations should be used for T_s <= 1170°C only. For T_s > 1170°C, there are no primary γ' particles.

- Secondary γ' microstructure formation during quench
  - Particle number density (1/m^3) at end of quench (note: the same with right after nucleation), $N_2(T_S, \dot{T})$, is described by

$$\log_{10}(N_2(T_S,\dot{T})) = 34.48352 + 1.53409\log_{10}(\dot{T}) - 0.01288\,T_S \qquad Eq.\ 9$$

  - Nucleation temperature (in °C),

$$T_{nuc}(T_S,\dot{T}) = 476.40 + 450.42\log_{10}(\dot{T}) + 0.55588\,T_S - 0.38888\,T_S\log_{10}(\dot{T}) - 194.478\,f_{\gamma'}^{eq}(T_S) \qquad Eq.\ 10$$

  - Initial particle radius (in meter) from nucleation,

$$R_2^0(T_S,\dot{T}) = \left[-1002.12 + 705.84\log_{10}(\dot{T}) + 0.9310\,T_S - 0.6551\,T_S\log_{10}(\dot{T})\right] \times 10^{-9} \qquad Eq.\ 11$$

  - After nucleation, particle radius growth equation is provided in differential form, following the continuous cooling temperature profile $T(t)$

$$\frac{dR_2(T(t))}{dt} = \frac{A_0}{R_2}\exp\left(-\frac{Q}{T(t)+\Delta K}\right) \qquad Eq.\ 12$$

$$\text{With } A_0 = 1.9250\times 10^{-5}, \qquad Q = 35648.43, \qquad \Delta K = 273.15$$

Where initial condition is specified when temperature just reaches T_{nuc} ($R_2(T_{nuc}) = R_2^0$)

  - With linear cooling, $T(t) = T_{nuc} - \dot{T}\,t$ (in °C), where time t is zero at $T = T_{nuc}$, the result of above differential equation can be approximated with

$$R_2(T(t)) = \left\{(R_2^0)^2 + \frac{2A_0}{Q^2\dot{T}}\left[\exp\left(\frac{-Q}{T_{nuc}+\Delta K}\right)(Q-2(T_{nuc}+\Delta K))(T_{nuc}+\Delta K)^2 - \right.\right.$$
$$\left.\left.\exp\left(\frac{-Q}{T_{nuc}-\dot{T}t+\Delta K}\right)(Q-2(T_{nuc}-\dot{T}t+\Delta K))(T_{nuc}-\dot{T}t+\Delta K)^2\right]\right\}^{\frac{1}{2}} \qquad Eq.\ 13$$

  - With above equation for linear cooling, the final radius after quench can be computed directly:

$$R_2 = \left\{(R_2^0)^2 + \frac{2A_0}{Q^2\dot{T}}\left[\exp\left(\frac{-Q}{T_{nuc}+\Delta K}\right)(Q-2(T_{nuc}+\Delta K))(T_{nuc}+\Delta K)^2 - \right.\right.$$
$$\left.\left.\exp\left(\frac{-Q}{T_{nuc}-\Delta T+\Delta K}\right)(Q-2(T_{nuc}-\Delta T+\Delta K))(T_{nuc}-\Delta T+\Delta K)^2\right]\right\}^{\frac{1}{2}} \qquad Eq.\ 14$$

Where ΔT is chosen as 300°C, representing the end of particle growth below T_{nuc}. With the determined Q parameter, results of final size is insensitive when $\Delta T >= 250$°C.

26

- Volume fraction of secondary particles can be computed with following equation:

$$f_2 = \frac{4\pi}{3} R_2{}^3 N_2$$

Eq. 14

- The above equations for secondary γ' prediction are applicable for $T_s <= 1175^{\circ}$C. For cases with $T_s > 1175^{\circ}$C, 1175°C is used in the above equations.

Calculated results using fast action model in comparison with PrecipiCalc results:

- Secondary γ' particle size and volume fraction vs. time as follows in Figure 33.
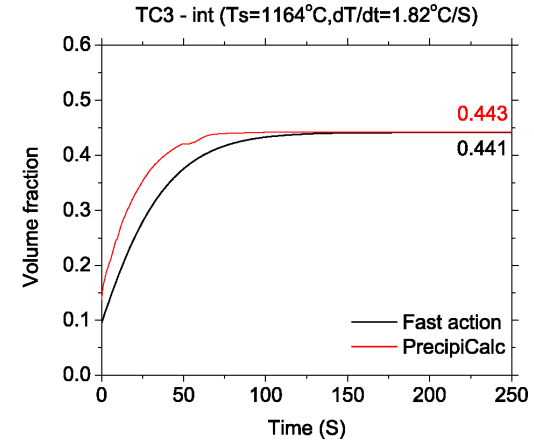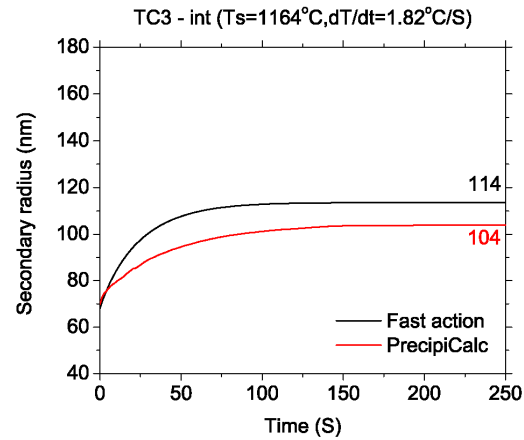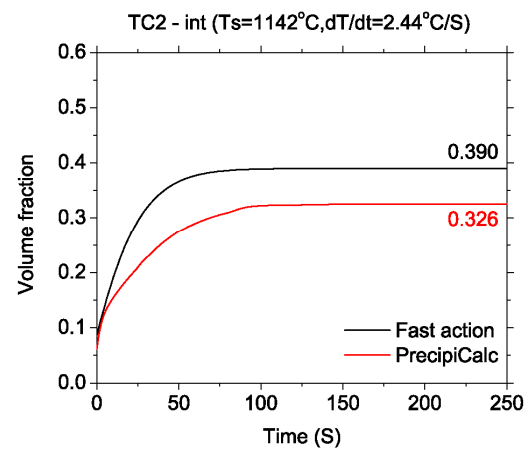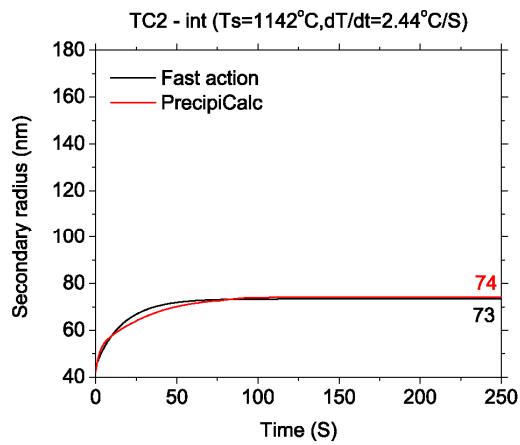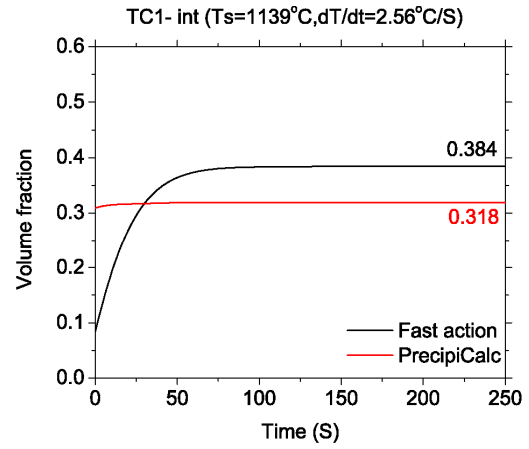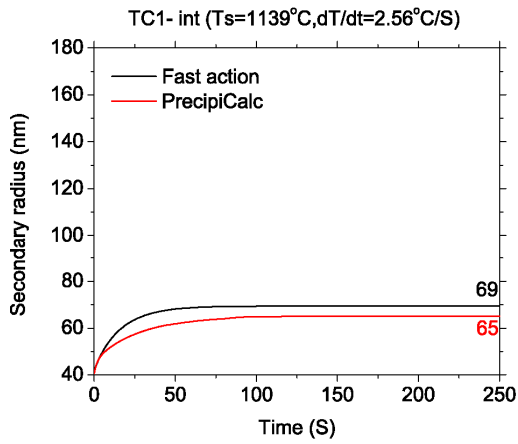
Figure 33. Secondary γ' particle size and volume fraction vs. time
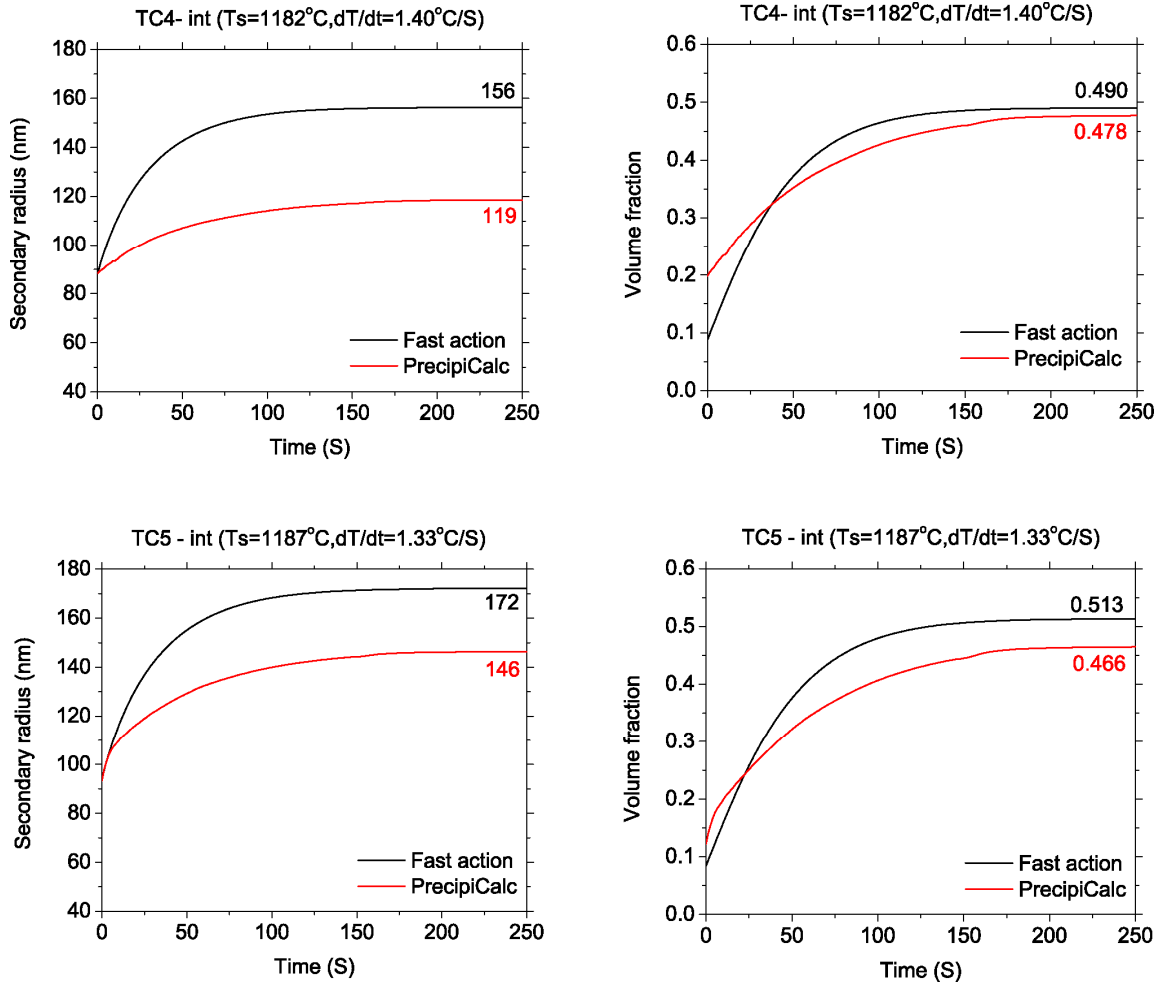
Figure 34. Size and volume fraction of secondary gamma prime particles as predicted by PrecipiCalc.

2.3 Property prediction from microstructure

2.3.1 Flow Stress - DEFORM Interpolated look-up-table

The DEFORM system has been enhanced during this project to include a tabular flow stress definition which utilizes microstructure as input. In addition to the typical function variables for flow stress (temperature, strain, strain rate), new variables such as grain size, particle size, particle shape, particle volume fraction, and more, can now add to the flow stress response surface. In this way, if a user has data which describe the response of a material's flow stress as a function of grain size or precipitates, then this information may be provided to the new microstructure flow stress tabular model. When computing local flow stress, this model will interrogate the local variables of each element in the workpiece (strain, strain rate, temperature, grain size, precipitate size, precipitate volume fraction, etc) and return the appropriate value for flow stress. As the underlying

microstructure features evolve (e.g. as grains refine during recrystallization, or enlarge during grain growth; or as precipitates emerge during cooling below the solvus temperature) then the local flow stress too will change. In this manner, processing and service conditions influence microstructure evolution, which in turn influence material physical properties.

2.3.2 Northwestern University Strength Model

In addition to the tabular flow stress model which utilizes microstructural data as input, Northwestern University provided a strength model as a function of specific physical phenomena. This model is derived from Tresa Pollocks' nickel-base superalloy strength model.

Strengthening model:

$$\sigma_{i,y} = \sigma_{i\gamma}\ (T)(\Sigma_i{}^{\blacksquare}d\sigma/\sqrt{(dC_ii)}\ \sqrt{(C_ii)}) + (1 - f_{i}p)\ h_{i}y^{i}\gamma\ \ 1/\sqrt{(d_{i}\gamma)}$$

$$+ f_{i}y\ k_{i}y^{i}(\gamma^{h})\ \ 1/\sqrt{(d_{i}(\gamma^{i})}) + M(1 - f_{i}P)[(\Gamma/2b)^{T}(1.5)\ \sqrt{((2bd_{i}s\ (f_{i}s/l - f_{i}P\ )/T_{i}L\ ) + 4/\pi^{i}(1.5)}\ - \Gamma(f_{i}s$$

$$+ M(1 - f_{P})\left|\frac{4}{\pi^{1.5}}\frac{T_{L}}{bd_{s}} + \left(\frac{f_{s}}{1 - f_{p}}\right)^{1.5}\sqrt{\frac{\pi d_{s}\Gamma_{APB}}{2T_{L}} - 1}\right|(30nm < d_{\gamma'} < 1000nm)$$

$$+ f_{P}\left|\sigma(T)_{Ni_{3}Al} + \sum_{i}\frac{d\sigma}{C_{i}}C_{i}\right|(d_{\gamma'} > 1000nm) \qquad\qquad Eq.\ 15$$

1. Solid solution strengthening of γ matrix

A superposition of strengthening of individual solutes that individually have differing potencies.

$$\sigma_{y} = \sigma_{\gamma}(T)\left(\sum_{i}\frac{d\sigma}{\sqrt{dC_{i}}}\sqrt{C_{i}}\right) \qquad\qquad Eq.\ 16$$

where σ_{γ} is function of temperature, $\frac{d\sigma}{\sqrt{dC_{i}}}$ is the strengthening coefficient that reflects the strengthening potency of each element, which can be taken from the table below.

Table 2. Strength per percent of alloying elements

Units	Al	Cr	Co	Mo	Ti	V	W	Nb	Ta	Zr
MPa/pct$^{1.5}$	225	337	39.4	1015	775	408	977	1183	1191	2359

$$\sigma_{\gamma}(T) = 0.99558 - 6.97474E - 5T - 1.92665E - 6T^{2} + 5.30617E - 9T^{3} - 4.27057E - 12T^{4} \quad Eq.\ 17$$

The units of T are ^{o}C.

2. Grain size strengthening of γ matrix and γ' phase

$$\sigma_y = (1 - f_p) k_y^\gamma \frac{1}{\sqrt{d_\gamma}} + \frac{2}{3} f_p k_y^{\gamma'} \frac{1}{\sqrt{d_{\gamma'}}}$$ *Eq. 17*

where k_y^γ and $k_y^{\gamma'}$ are the Hall-Petch constant for γ matrix and γ' phase, f_p is the phase fraction of γ' phase, and d_γ and $d_{\gamma'}$ are the grain size of γ matrix and γ' phase.

- k_y^γ=750 MPa/μm
- $k_y^{\gamma'}$ =500 MPa/μm
- d_γ =34.4 μm

3. shearing/bowing of secondary γ' strong pair coupling $(d_{\gamma'} < 30nm)$

$$\sigma_y = M(1 - f_P)\left[\frac{4}{\pi^{1.5}}\frac{T_L}{bd_s} + \left(\frac{f_s}{1-f_p}\right)^{1.5}\sqrt{\frac{nd_s\Gamma_{APB}}{2T_L}} - 1\right]$$ *Eq. 18*

T_L is calculated using the equation below.

$$T_L = \frac{Gb^2}{4\pi}\left(\frac{1 - v\cos^2\theta}{1-v}\right)\ln\left(\frac{R}{r_0}\right)$$ *Eq. 19*

Where G is the shear modulus (=76 GPa); v is the Poisson's ratio (=0.3); θ (=60°)is the angle between the dislocation line and its Burgers vector b (=2.5Å); R is the outer cutoff distance (=10 nm), which is approximately the distance to the closest parallel dislocation of the opposite sign; and r_0 is the inner cutoff radius, taken to be b. Γ_{APB} is the antiphase boundary energy (=0.20 J/m^2). M is the Taylor factor of fcc (=3).

4. shearing/bowing of tertiary γ' strong pair coupling $(30nm < d_{\gamma'} < 1000nm)$

$$\sigma_y = M(1 - f_P)\left[\left(\frac{\Gamma_{APB}}{2b}\right)^{1.5}\sqrt{\frac{2bd_s\left(\frac{f_s}{1-f_p}\right)}{T_L}} + \frac{4}{\pi^{1.5}} - \frac{\Gamma_{APB}\left(\frac{f_s}{1-f_p}\right)}{2b}\right]$$ *Eq. 20*

5. Cross-slip-induced strengthening of γ' phase $(d_{\gamma'} > 1000nm)$

$$\sigma_y = f_P\left[\sigma(T)_{Ni_3Al} + \sum_i \frac{d\sigma}{C_i}C_i\right]$$ *Eq. 21*

where $\sigma(T)_{Ni_3Al}$ is the strength of pure Ni3Al as a function of temperature, C_i is the concentration of the ith alloying element. In the model, cross-slip-induced hardening occurs in primary γ' and secondary γ' precipitates larger than 300 nm. An APB energy of 200 mJ/m^2.The value of $\frac{d\sigma}{C_i}$ can taken from the table below.

Table 3. Strength per percent of alloying elements with respect to particle shearing

Units	Al	Cr	Co	Mo	Ti	V
MPa/pct	0	7	0	16.8	25	8.2

$$\sigma(T)_{Ni_3Al} = 106.99392 + 0.13442T + 7.42125E - 4T^2 + 2.46519E - 6T^3 - 3.79348E - 9T^4 \qquad Eq.\ 22$$
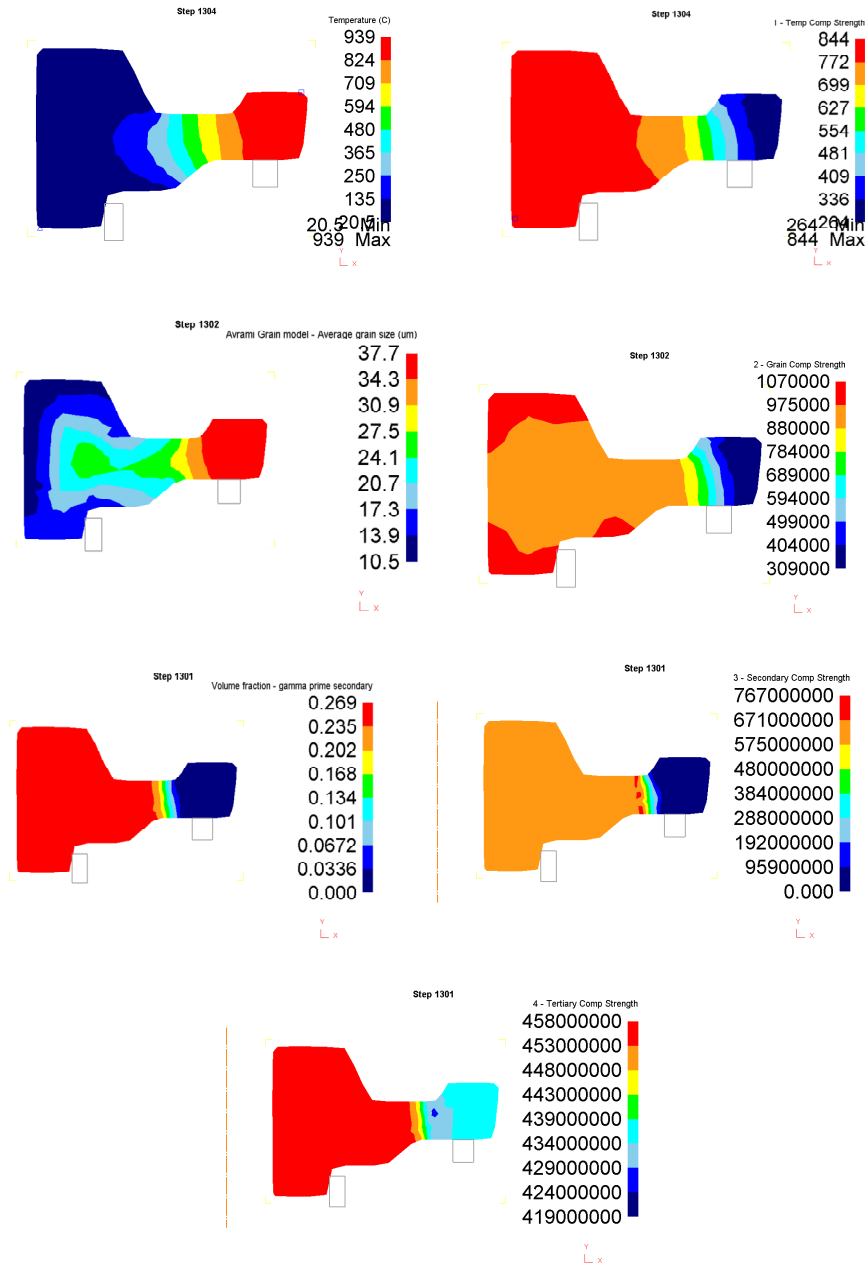
(MPA) with T (^{o}C)

Figure 35. Components of strength due to underlying microstructural phenomena.

Note that the fine grained region provides the strongest overall strength; the coarse grained region provides the lowest overall strength. Variation of volume fraction of gamma prime primary, secondary, and tertiaries contribute to the rest of the strength.

2.3.3 Creep

Creep properties for LSHR are available in the NASA report by Gabb and Gayda of 2006[4]. Microstructural influence on creep resistance can be defined by grain size and presence of second phase. Large grains mean less grain boundary sliding; and a distribution of fine precipitates pins dislocations and produces a "back stress" threshold to overcome before creep initiates. Two separate models can predict the effect of these phenomena - the Dorn model, which predicts creep strain rates as a function of grain size, and the Langdon model[9], which predicts creep strain rates as a function of size and volume fraction of second phases. These are both discussed below.

Rather than incorporating both into a hybrid model to predict creep strain rates in DEFORM, the creep strain rate model was enhanced to also be a function of microstructure features. An industrial user is then encouraged to perform calculations external to DEFORM to produce a "look up table" of creep strain rates as functions of underlying microstructure (grain size, precipitates) as well as state variables (strain, stress). This look up table can then be entered into a new DEFORM creep algorithm which is a function of microstructure, and the creep strain rate at each element in the virtual DEFORM workpiece is thus a function of the microstructure and state variables present at that element. In this manner, creep strain rates may locally be computed as a local function of prior processing and microstructure evolution.
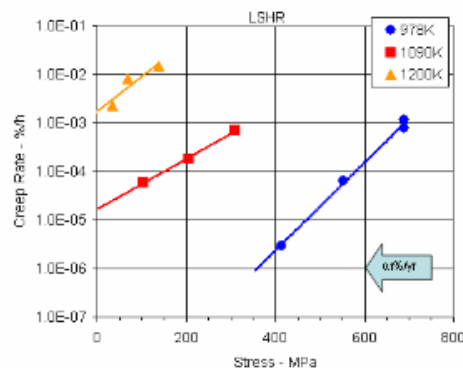

Figure 36. Creep data for LSHR at 3 different temperatures and a range of stresses, from NASA Report[4].

Multiple microstructure-related creep models exist to correlate creep strain rate to grain size, volume fraction and size of precipitates, and more. Two such models are the Dorn model and the Langdon model, below.

2.3.1.1 Dorn Model

The Dorn model correlates the effect of precipitates on creep strain rate[10]. Fine precipitates pin dislocations and prevent creep from occurring unless the applied stress is sufficient to exceed the "back stress" that pinning precipitates apply to dislocations. This is manifested in Equation 23 in the form of a threshold backstress (σ_b) that must be exceeded by the applied stress (σ_a). Otherwise, this term is set to zero.

$$\dot{\varepsilon} = A \left(\frac{\sigma_a - \sigma_b}{E} \right)^n \exp\left[-\frac{Q_{real}}{RT} \right] \qquad\qquad Eq.\ 23$$

Note that this formulation is relevant for a constant volume fraction and size of precipitates. If the volume fraction varies, then it is necessary to inform the equation with a variable that accounts for the volume fraction. This was proposed during the initial progress in this project, and is documented in previous progress reports. For this formulation, a "normalized volume fraction" variable is used to correlate the creep strain rate to varying values of volume fraction of pinning precipitates.

$$\dot{\varepsilon} = NVF * A \left(\frac{\sigma_a - \sigma_b}{E} \right)^n \exp\left[-\frac{Q_{real}}{RT} \right] + (1 - NVF) * A \left(\frac{\sigma_a}{E} \right)^n \exp\left[-\frac{Q_{real}}{RT} \right] \qquad Eq.\ 24$$

However, this formulation can grow unwieldy, especially when enhanced to include grain size effects as well (discussed next). Thus, the final implementation of creep strain rate as a function of microstructure integrated into DEFORM as a result of this program is to add additional dimensions to the tabular look-up-table method of interpolating creep strain rate amongst relevant state variables - stress, strain, temperature, grain size, precipitate size, precipitate volume fraction, and more. This is discussed later.

2.3.1.2 Langdon Model

The Langdon model correlates creep strain rate to grain size, by including the grain size term in the denominator of the creep strain rate equation. Thus, the larger the grain size, the smaller the creep strain rate, as is the case when grain boundary sliding is the mechanism for creep.

$$\dot{\varepsilon} = \frac{ADGb}{kT} \left(\frac{b}{d} \right)^p \left(\frac{\sigma}{G} \right)^n \qquad\qquad Eq.\ 25$$

Similar to the prior model, this equation requires enhancement when integrating other microstructure features such as precipitate size, volume fraction, shape, etc. Rather than producing an unwieldy and difficult-to-validate creep strain rate model which is a mix of these two, as stated earlier, the creep strain rate model integrated into DEFORM for this project rather allows a user to add additional dimensions to tried-and-true creep strain

rate models which inform the creep strain rate with the effect of evolving grain size, precipitate size, etc.

2.3.1.3 Integrated grain size and precipitation model

A new creep strain rate model was created for DEFORM during this project that allows a user to correlate creep strain rate to the conventional state variables (stress, strain, temperature, time) but also allows the model to be influenced by microstructure features such as grain size, precipitate size, and more. This model is effectively a look-up-table that interpolates amongst the various relevant ranges of state variable values, and computes the creep strain rate appropriate for the particular microstructural condition and state variable combination at each element in the workpiece.

Thus, a user should "pre-process" the response surface of creep strain rate as a function of relevant state variables and microstructure features, and then input this in tabular format into DEFORM. An example is provided below.

For example - Figure 37 displays the effect of stress and temperature on creep strain rate in LSHR. Fitting the Langdon model to this data, one can obtain the creep response of a spin pit test displayed in Figure 42.
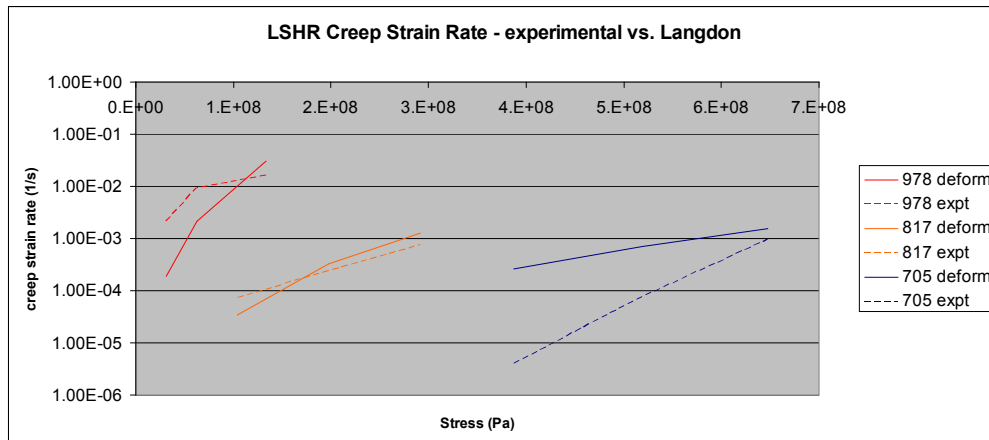
Figure 37. Creep strain rate as a function of temperature and applied stress, for experimental data (from Figure 36) and results from fitted Langdon equation.

Note that fitting the Langdon equation does not result in a very good match for the low temperature regime. These constants were fitted manually, and this process could benefit from inverse analysis of tuning constants - a process being developed for DEFORM in other related projects.

$$\dot{\varepsilon} = \frac{ADGb}{kT}\left(\frac{b}{d}\right)^{p}\left(\frac{\sigma}{G}\right)^{n}$$ *Eq. 26*

35

Table 4. Constants fitted to the Langdon equation for LSHR.

Q	D_0	D	A	G(Pa)	b (μm)	d	p	n
200000	1.00E+00	4.45489E-09	1.20E+01	1.88E+10	2.50E-09	3.00E-05	2.00E+00	3.50E+00

where k is the Boltzmann constant, T is the local temperature, and σ is the local applied stress.

2.4   Constant load creep modeling

Constant load creep tests are often utilized to determine the creep strain rate response of a material to stress, strain, temperature, microstructure, and more.   A creep test involves a tensile specimen under a constant load maintained at a constant temperature; strain measurements are then recorded over a period of time.

Creep often occurs in three stages: primary, or stage I; secondary, or stage II: and tertiary, or stage III. Stage I creep occurs at the beginning of the tests, and creep is mostly transient, not steady rate. Resistance to creep increases until Stage II is reached, at which point the rate of creep becomes largely steady, and is often referred to as steady state creep. In Stage III creep, the creep rate begins to accelerate as the cross sectional area of the specimen decreases, either due to necking of the specimen or formation of internal voids, which decreases the effective area of the sample. If stage III is allowed to proceed, fracture will occur.

The creep test is usually employed to determine the minimum creep rate in stage II, which is necessary to take into account when designing components to operate at elevated temperatures under load, such as aviation turbine disks.
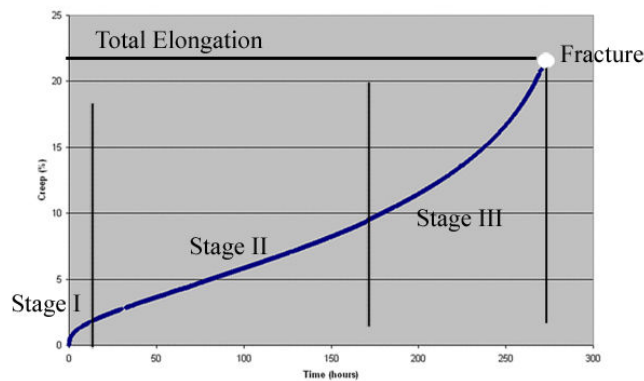
Figure 38. Three stages of creep.

2.4.1 Creep Testing

A virtual creep test begins with an elastoplastic coupon, and an initial prescribed displacement which strains the sample and maintains it under constant load. Creep strain rate is then computed via one of the multiple creep models in DEFORM; for this program, the tabular creep strain rate utilizing microstructural inputs was modeled.
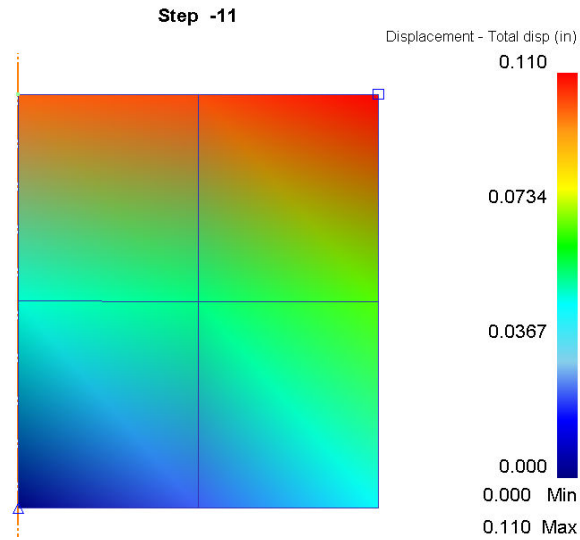
Figure 39. Virtual test coupon used for creep strain rate testing.
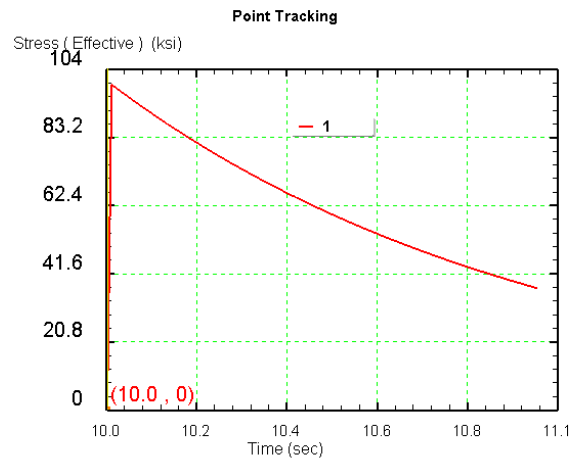
Figure 40. Decay of stress during constant-load simulated creep test.
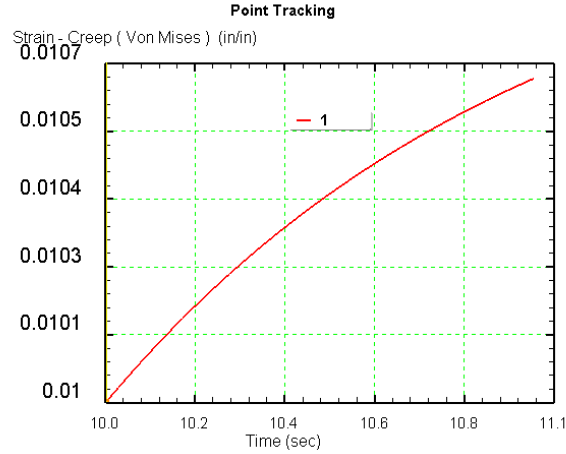
Figure 41. Increase in creep strain during constant load simulated creep test.

2.4.1.1 Interpolated look-up-table

As stated earlier, rather than producing a new model of creep which integrates both grain size and precipitate size and volume fraction, additional dimensions related to microstructure were added to the tabular creep strain rate model in DEFORM. This process is described below.

The value of *d* (grain diameter) used above in section 2.3.2.3 was ~20 microns. The results from this fitting were then tabularized as functions of stress, temperature, and grain size. The value of *d* was then changed to 4.5 microns and again to 35 microns (the values of the grain sizes present in the DMHT disk of Figure 32), and the results tabularized. In this way, a response surface of creep strain rate as a validated fit to experimental data for temperature and stress may be derived, and enhanced with physics-based impact of different grain sizes.

The same can be done to apply the effect of the presence of precipitates; if data are available to correlate both the size and the volume fraction of the precipitates, then these data may also be tabularized to produce a calibrated and physics-based response surface of creep strain rate as a function of natural creep variables (temperature, time, stress) and also of underlying local microstructure features (precipitate diameter, number density, shape, etc).

This data was then provided to the new microstructural model of creep integrated into DEFORM as a result of this project, and simulated spin tests were performed. The non-recoverable deformation above and beyond elastic displacement (e.g. plastic deformation, creep strain deformation) is then exclusively a function of the validated and physics-based evolution of flow stress and/or creep strain rate influenced by local state variables and microstructural features.

These sets of tabular data are multi-dimensional, and thus difficult to represent in 2D or 3D figures. Thus, the tabular data itself are presented below. Values in bold are the data provided to the DEFORM simulation. For completeness' sake, comments in *parentheses* are included, and are a description of how the data are converted to creep strain rate during a DEFORM simulation.

CREEP 1 7 *(material # 1, the mixture material, obeys the tabulated creep strain rate data as f(microstructure))*
3 *(# variables to interpolate creep strain rate across)*
4 3 0 *(variable "3", stress, has 4 values of the "x" array)*
2 6 1 *(variable "6", grain size, has 2 values in "x", and applies to Material 1 (average grain size))*
3 7 3 *(variable "7", precipitate size, has 3 values in "x", and applies ot Material 3 (gamma prime primary))*
0.0 30.0 40.0 200.0 *(stress values in "x" are 0 MPa, 30 MPa, 40 MPa, and 200 MPa)*
4.5 35 *(grain size values in "x" are 4.5 microns and 35 microns)*
6.0e-7 6.6e-7 1.2e-5 *(precipitate size values in "x" are 0.6 microns, 0.66 microns, and 12 microns)*
0 0 1.11e-9 2.22e-8   *(determine strain rate in "y" for grains = 4.5 microns, ppt size = 6e-7, and interpolate stress)*
0 0 1.11e-10 2.22e-9   *(determine strain rate in "y" grains = 35 microns, ppt size = 6e-7, and interpolate stress*
0 0 1.11e-9 2.22e-8   *(determine strain rate in "y" grains = 4.5 microns, ppt size = 6e-6, and interpolate stress*
0 0 1.11e-10 2.22e-9   *(determine strain rate in "y" grains = 35 microns, ppt size = 6e-6, and interpolate stress*
0 0 1.11e8- 2.22e-7   *(determine strain rate in "y" grains = 4.5 microns, ppt size = 1.2e-5, and interpolate stress*
0 0 1.11e-9 2.22e-8   *(determine strain rate in "y" grains = 35 microns, ppt size = 1.2e-5, and interpolate stress*
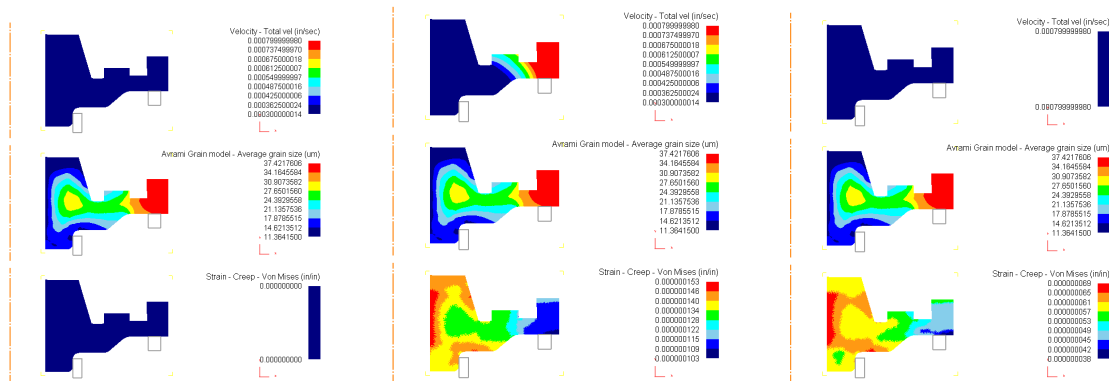
Figure 42. Top - velocity of a disk during simulated spin test; center - grain size; bottom - accumulated creep strain. Left - beginning of test; middle - middle of test; right - end of test.

2.4.1.2 Bauschinger effect

Some metals shows the Bauschinger effect during the tension and subsequent compression test shown in Fig. 38. Therefore it is essential to model the Bauschinger effect correctly when material points are subjected to cyclic loading conditions. The combined nonlinear hardening model for time independent cyclic plasticity, proposed by Chaboche and co-workers, is popularly used for metal plasticity. This model represents the isotropic hardening behavior and kinematic hardening by expansion and translation of the yield surface. This combined behavior for the uniaxial tensile condition can be illustrated in Figure 39. Three different hardening models are compared with the uniaxial cyclic loading case, for example tension-compression-tension, in Figures 40 and 41.

The combined iso-kinematic hardening model exhibits a more realistic response.

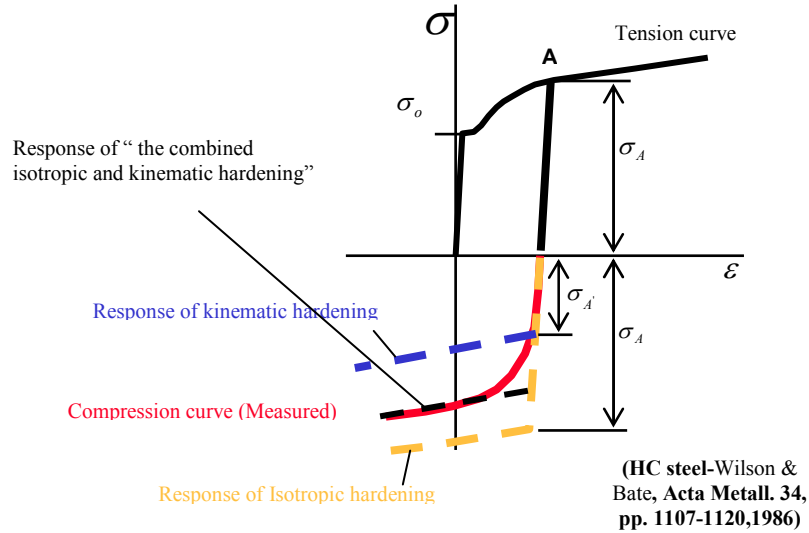Figure 43. Typical Bauschinger curves under tension and subsequent compression loading; (Black: measurement, Red: combined model, Orange: isotropic model with no Bauschinger effect, Blue: kinematic model)

Key equations for translation of the yield surface follow.

$$f = \frac{1}{2}(\boldsymbol{\sigma} - \boldsymbol{\alpha})^{\mathrm{T}} \mathbf{A}(\boldsymbol{\sigma} - \boldsymbol{\alpha}) - (\sigma^{o})^{2} = 0$$

Where

$$\mathbf{A} = \begin{bmatrix} \beta_{11} & -\beta_{12} & -\beta_{13} & 0 & 0 & 0 \\ -\beta_{12} & \beta_{22} & -\beta_{23} & 0 & 0 & 0 \\ -\beta_{13} & -\beta_{23} & \beta_{33} & 0 & 0 & 0 \\ 0 & 0 & 0 & \beta_{44} & 0 & 0 \\ 0 & 0 & 0 & 0 & \beta_{55} & 0 \\ 0 & 0 & 0 & 0 & 0 & \beta_{66} \end{bmatrix}$$

Linear kinematic model :

$$\dot{\boldsymbol{\alpha}} = \frac{C}{\sigma^{o}}(\boldsymbol{\sigma} - \boldsymbol{\alpha})\dot{\bar{\varepsilon}}^{p}$$

The combined model*:

$$\dot{\boldsymbol{\alpha}} = \frac{C}{\sigma^{o}}(\boldsymbol{\sigma} - \boldsymbol{\alpha})\dot{\bar{\varepsilon}}^{p} - \gamma(\boldsymbol{\alpha})\dot{\bar{\varepsilon}}^{p}$$
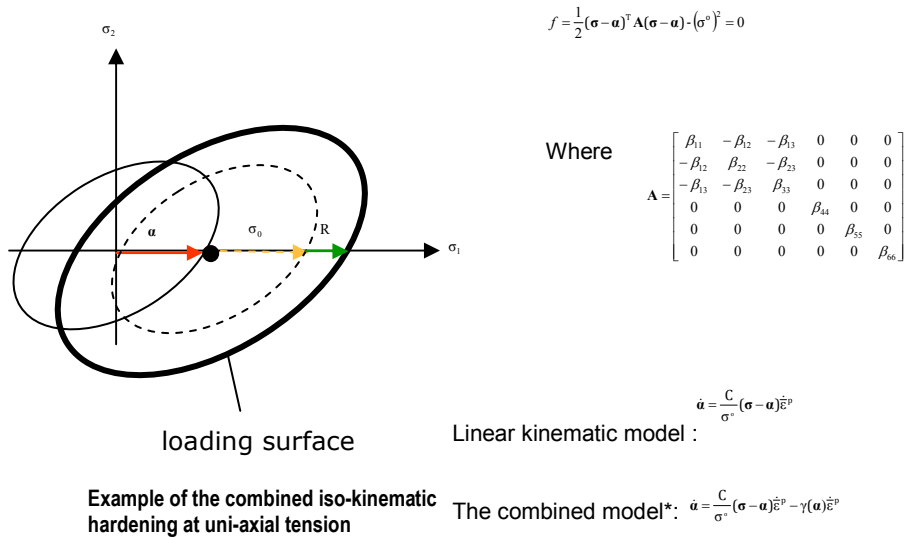
*Original idea developed by Chaboche(1986): Int. J. of plasticity,p149

Figure 44. Example of uniaxial tensile loading.

An example of uniaxial tensile loading is demonstrated in Figure 40.

$$\sigma = 100 + H\bar{\varepsilon}^p$$

$$\alpha = H\bar{\varepsilon}^p$$

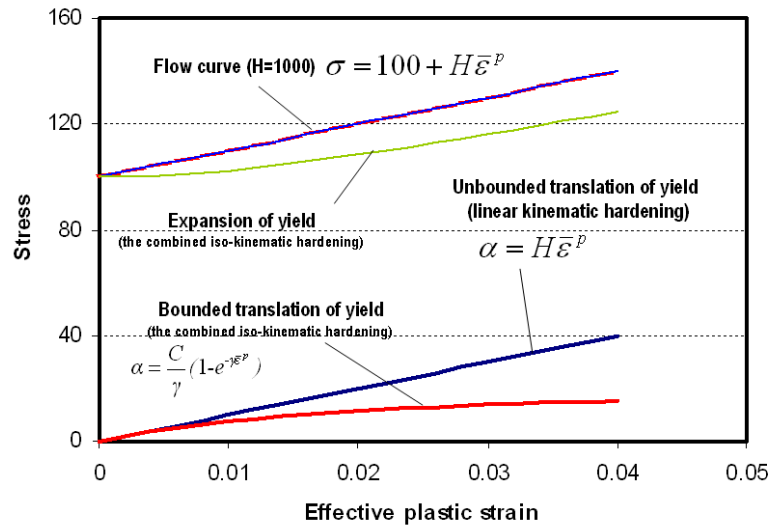$$\alpha = \frac{C}{\gamma}(1 - e^{-\gamma\varepsilon^p})$$

Figure 45. Back stress evolutions with kinematic hardening model and the combined iso-kinematic hardening model under uniaxial cyclic loading:

An example of uniaxial cyclic loading is presented in Figure 41.

• Material parameters

$$\sigma = 100 + H\bar{\varepsilon}^p$$
$$E = 200\,GPA$$
$$v = 0.3$$
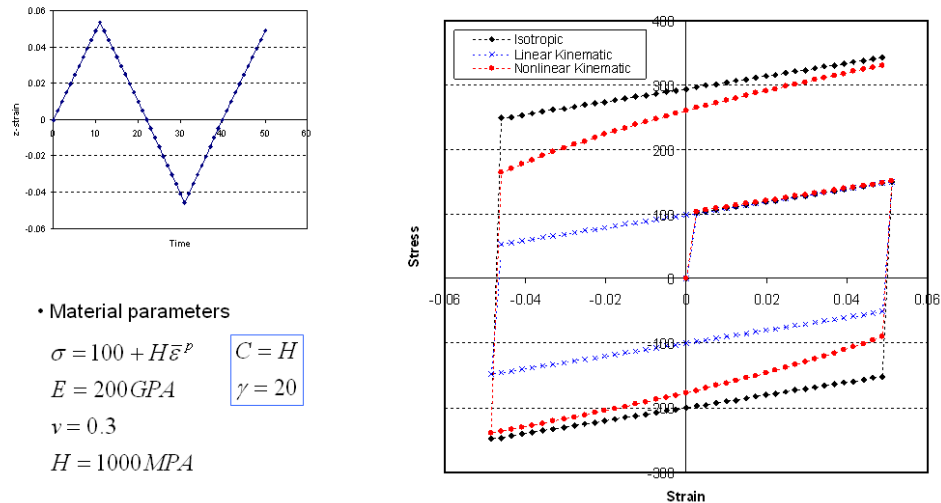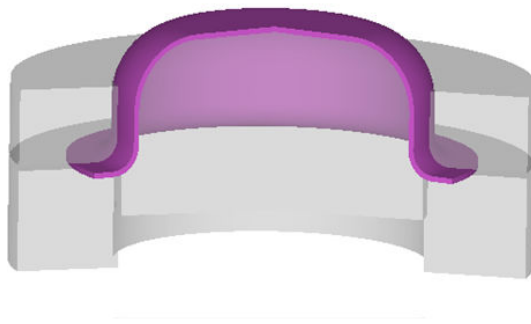$$H = 1000\,MPA$$

$$C = H$$
$$\gamma = 20$$

Figure 46. Stress evolutions with isotropic, kinematic hardening and the combined iso-kinematic hardening model under uniaxial cyclic loading:

To demonstrate the effect of the combined iso-kinematic hardening model in a real metal forming simulation, the assumed parameters for the model used are shown in Figure 42.

In Figure 43, two typical locations were examined using the point-tracking method. It is shown that for material points which were tracked under compression and tension, such as in cyclic loading, a much lower punch force of two kinematic hardening models results. For the punch force comparison, the combined iso-kinematic model is between isotropic hardening and kinematic hardening model shown in Fig.44.

• Material parameters

$$\sigma = 100 + H\bar{\varepsilon}^p \qquad \boxed{C = H}$$

$$E = 200\,GPA \qquad \boxed{\gamma = 20}$$

$$v = 0.3$$
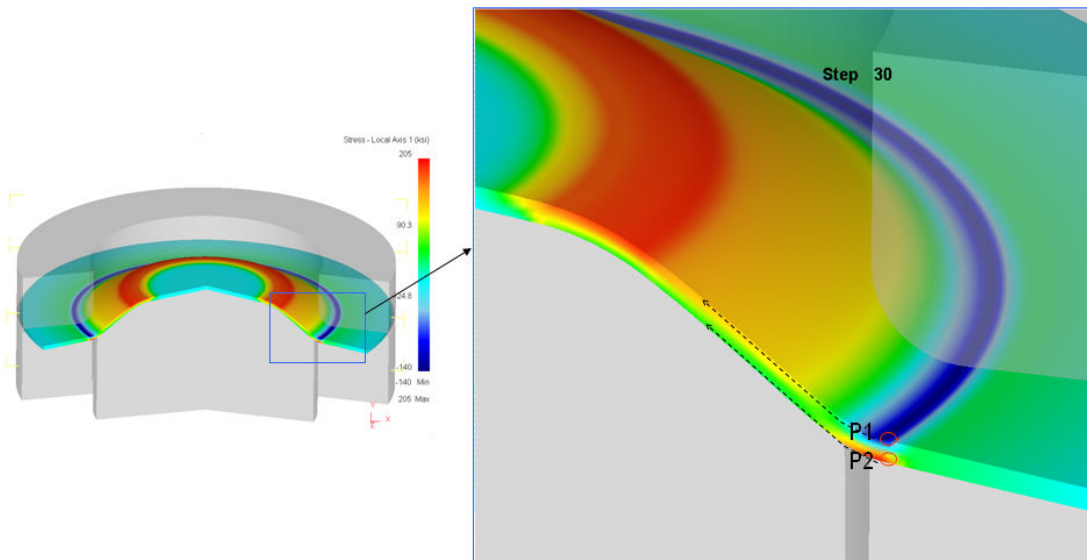
$$H = 1000\,MPA$$

Figure 47. Cup drawing.

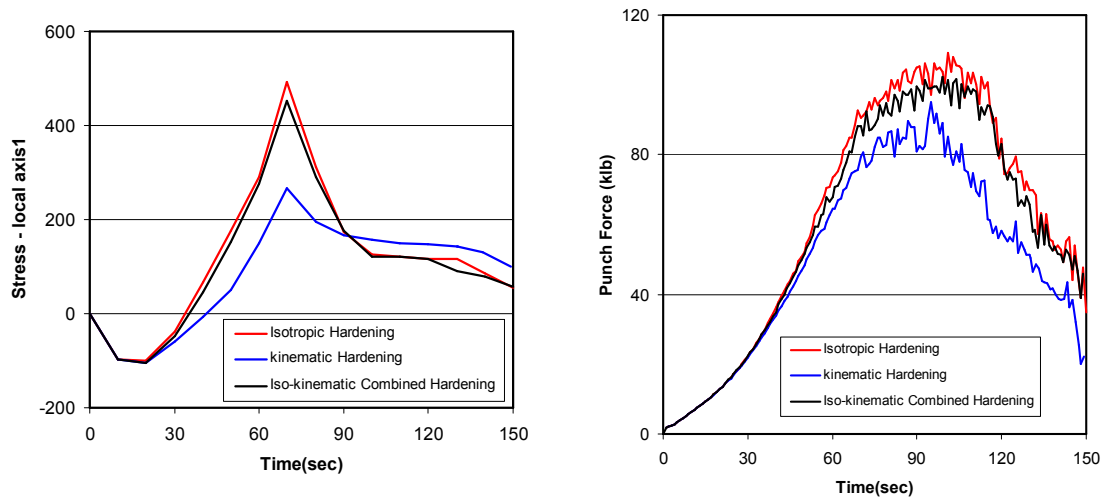Figure 48. Point tracking of stress with respect to local material axis.

Figure 49. Point tracking of stress (with respect to local material axis) and punch loads.

Identification of material parameters associated with a selected plasticity model is a critical issue for finite element simulations. Several options for direct or indirect measurement of metal sheets are possible; two examples are shown in Figure 45 and 46. One is curve fitting tension-compression (or compression-tension) test data with different pre-strains and the other is inverse calculation from three-point bend tests. (Figure 45 shows the example of three-point bend tests and Figure 46 shows the comparisons of identification curves with two methods.).
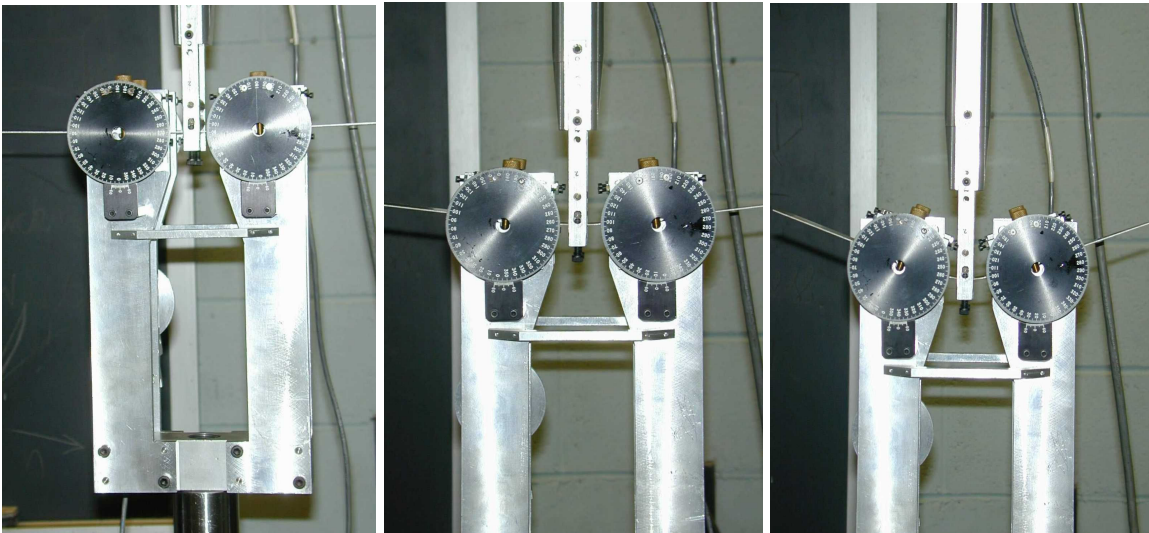

Figure 50. One of the possible measurements; a 3-point bending test (J.K. Lee and R.H. Wagoner, OSU).
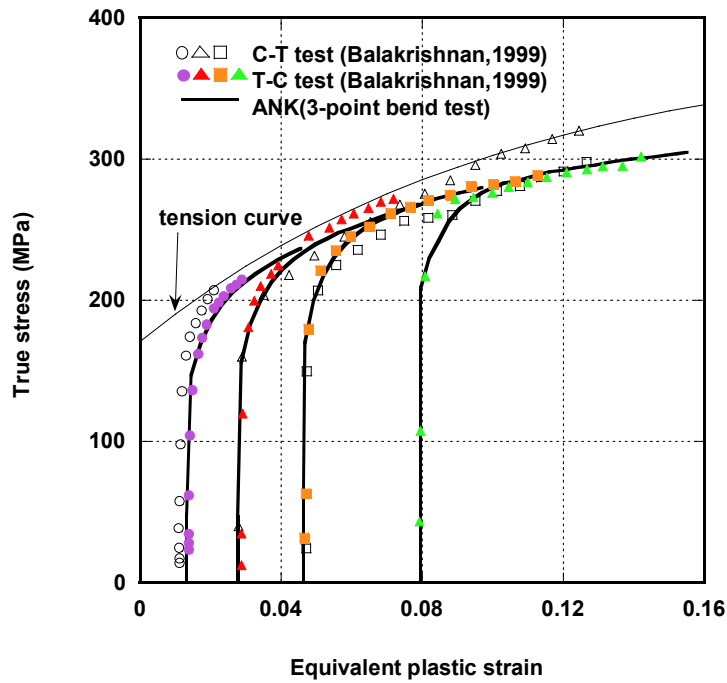
Figure 51. Determination of material parameters via tension-compression cyclic tests or bending-rebending cyclic tests.

Table 5. Simple Comparison of Various Hardening Models

Models	Isotropic hardening	Kinematic hardening	The combined iso-kinematic hardening
Required Input	Flow curves	Flow curves	Flow curves + additional material parameter
kinetic of Yield surface	Expansion only	Translation only	Translation + Expansion
Representation of Bauschinger Effect	No	Yes, but good for only small deformation cases. Excessive representation at large deformation	Yes, good for both small and large deformation cases
Availability in DEFORM	Yes	Yes	Yes

A brief comparison summary of three different hardening models can be made in Table 5.

In the reference, material RR1000 also shows the Bauschinger curve which is demonstrated under cyclic loading conditions in Figures 47 and 48.

$$\sigma = 695 + 161.52(1 - e^{-7.13\bar{\varepsilon}^{p}})MPa$$

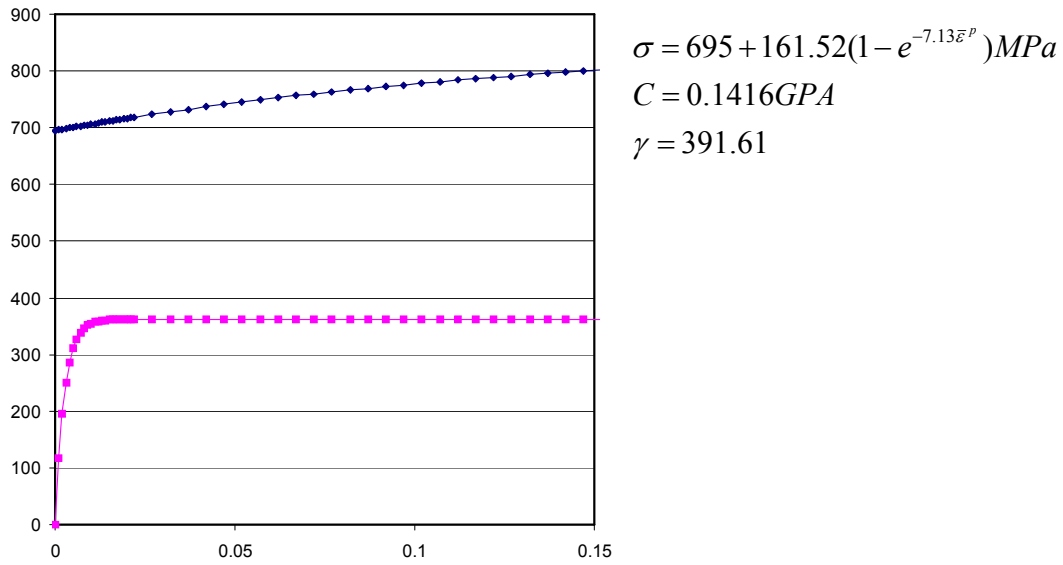$$C = 0.1416 GPA$$

$$\gamma = 391.61$$

Figure 52. Two different hardening models. (Reference: R. A. Claudio et al, "Crack Propagation Behavior of Shot Peened Components at Elevated Temperature", *Jornadas de Fractura*, Univ. do Minho, Portugal, 2006).
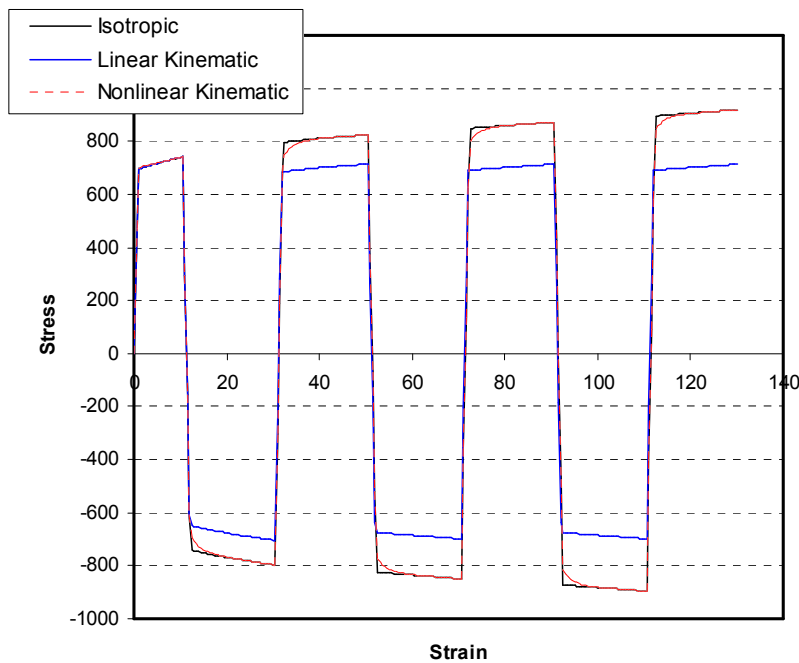
Figure 53. Tension-compression test for RR1000 material (Reference: R. A. Claudio et al, "Crack Propagation Behavior of Shot Peened Components at Elevated Temperature", *Jornadas de Fractura*, Univ. do Minho, Portugal, 2006).

2.5 Zener Pinning Model Refinement

Previous refinement under the DARPA-AIM program of grain boundary Zener pinning models to account for size distributions of multiple pinning phases (*e.g.* primary γ' and carbides) provided a function for the average 3D grain size D vs. a summation over the size distributions of particles. The model also incorporated a correction factor for the effect of total pinning phase fraction f_T, reflecting reduced pinning efficiency at high total fractions, as for the case of subsolvus treated disc alloys. More recent research under the ONR/DARPA "D3D" Digital Structure consortium used tomographic reconstruction methods to quantify departures of spatial distributions of particles from the common random uniform assumption. Analysis of the carbide spatial distribution in an IN100 aeroturbine disc superalloy showed the highest departure from random uniform as a result of particle clustering associated with extensive thermomechanical treatment under subsolvus conditions with respect to the γ' phase. Quantification of the nonuniformity allowed a correlation with the reduced pinning efficiency observed in supersolvus treated material where only the nonuniform carbides provide pinning. Under the current project we have synthesized all these results into one comprehensive pinning model allowing separate treatment of the pinning efficiency of γ' and carbides resulting from their differences in spatial uniformity. The comprehensive model is represented by

$$D = K_0 (1 + C_0 f_T^m) \left(\frac{C_1 \Sigma f_i}{d_i} + \frac{C_2 \Sigma f_j}{d_j} \right)^{-1}$$

Eq. 27

where

$K_0 = 0.227$
$C_0 = 13.7$
$m = 0.81$

In the second term, the f_i, d_i and f_j, d_j represent the fractions and sizes of the two different γ' and carbide populations and the C_1 and C_2 coefficients represent their relative pinning efficiencies associated with their degree of spatial nonuniformity.

Under the D3D project a "Spatializer-L" code was developed to analyze the spatial nonuniformity of tomographic datasets of particle arrays. The code is distributed as freeware through the D3D website now maintained by TMS. Analysis of a given tomographic particle distribution dataset computes the distribution of near neighbor spacings, and ultimately represents their departure from spatial uniformity by a single parameter, COV, which is the coefficient of variation of the spacing distribution defined by the ratio of the standard deviation to the mean of this distribution. The value of COV is 0 for an ordered array of particles, and 0.36 for a uniform random array. The small degree of clustering measured in a typical wrought alloy corresponds to a COV of 0.64, while the severe nonuniformity measured for the carbide array in the IN100 disc alloy corresponds to a COV of 0.97. Correlating the measured nonuniformity to the measured pinning efficiency in supersolvus treated IN100 gives a simple linear relation between pinning efficiency and spatial distribution COV. Thus the values of C_1 and C_2 in the grain size equation can be related to the measured COV values according to

$C_n = C_n^0 - C_n^1 (COV)$ 　　　　　　　*Eq. 28*
with $C_n^0 = 1.75$ and $C_n^1 = 1.50$.

For the relatively uniform γ' array, C_1 can be computed using COV=0.50, while for the highly nonuniform carbide arrays in typical disc alloys the C_2 coefficient can be evaluated using COV=0.97.

A common measure of grain size in disc alloys is the 2D equivalent area, giving an apparent average grain diameter D_A. This quantity can be related to the true 3D grain diameter D modeled here by the relation $D=1.25 D_A$.

2.6 Fatigue Life Modeling

The recent ONR/DARPA D3D Digital Structure consortium project also demonstrated a micromechanical approach to the modeling of heterogeneous fatigue nucleation on nonmetallic inclusions that dominate minimum fatigue life at high cycle (HCF) and ultrahigh cycle (UHCF) fatigue conditions in both cast/wrought and PM processed high strength alloys [1]. Within the approximation of local isotropic plasticity, the DEFORM-3D code can simulate the evolution of plasticity near observed high potency inclusion

clusters with meshes such as that depicted in Figure 54. As a worst case to represent minimum fatigue life, the particles in the inclusion cluster are treated as partially debonded normal to the maximum principal stress direction z, and given a higher elastic modulus appropriate to a nonmetallic inclusion. The overall flow strength is taken as the macroscopic strength predicted by our multiphase strengthening model. Retaining the approximation of isotropic plasticity, the softening effect of a worst case local crystal orientation can be represented by an isotropic strength knockdown factor of 2/3 based on the reciprocal product of the polycrystal Taylor factor and maximum single crystal Schmid factor. This then models the worst case of a potent damaged inclusion cluster located in a group of grains of high Schmid factor. The characteristic plastic field at this nucleant can then be computed by simulating the first 10 loading cycles at a given macroscopic stress or strain amplitude. Choosing a representative volume as outlined in red in Figure 54, the computed stress and strain distribution in this volume can be used to compute an average value of the Fatemi-Socie Fatigue Indicator Parameter (FIP) represented by:

$$P_{FS} = \frac{\Delta \gamma_{max}^{p*}}{2} \left(1 + K' \frac{\sigma_n^{max*}}{\sigma_y} \right) \qquad\qquad Eq.\ 29$$

Here, $\Delta \gamma_{max}^{(p*)}$ is the maximum plastic shear strain amplitude, while the coefficient K' takes into account the damaging effect of the local maximum normal stress σ_n^{max*} scaled to the local yield stress σ_y.

The computed FIP can then be correlated to an S-N fatigue life curve by setting the FIP equal to a Coffin-Manson parameter of the form $P_{FS}=\gamma_f(2N)^c$ where the coefficient γ_f and exponent c serve as fitting parameters.

In this way, the simulation of location-specific strength in a heat-treated component can be used to estimate the corresponding minimum fatigue nucleation life if a worst-case fatigue nucleant is located there.
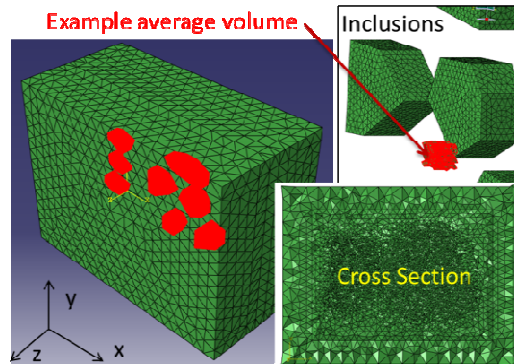

Figure 54. Gridded array of observed nucleating inclusions [RX6]. Interfaces are treated as partially debonded normal to z.

2.7 ATI Ladish - Industrial Component Modeling

In 2009, ATI Ladish Forging produced LSHR disks using the SuperCooler (Ladish patent) process under the US Air Force Contract FA8601-08-P-0291[7]. The objective of the project was to demonstrate the dual-microstructure on the LSHR material using the DMHT (Dual Microstructure Heat Treatment) technique. ATI Ladish successfully produced the disks by predicting and generating the dual-microstructure at the right location with coarsened grains at the rim while retaining the fine grain at the bore (Figure 55 and 56). Disks were delivered to the US Air Force as part of the contract.

DMHT technique is the key to the optimal distribution of grain size primarily balancing creep and strength requirement for an engine application. Another important element in the alloy strengthening is the gamma prime characteristics. Gamma prime (primary, secondary and tertiary) precipitates and evolves during the cooling of the disk. Characterization of gamma prime (γ') is equally important to determine the disk's tensile strength that influences the performance and life in an engine environment. This project work is to predict the gamma prime distribution in a LSHR disk.

Scientific Forming Technologies Corporation (SFTC, DEFORM parent) sub-contracted this work to ATI Ladish Forging to predict the gamma prime evolution and its characteristics in the supplied LSHR disc. This was part of the STTR Phase II project awarded to SFTC by USAF and endorsed by ATI Ladish. ATI Ladish was provided with PrecipiCalc™ to perform this predictability. Particle size distribution and kinetics of gamma prime evolution in the LSHR alloy were provided by QuesTek to Ladish. Ladish's proprietary thermal models were used to capture the cooling path and predict the gamma prime distribution (primary, secondary, tertiary) at the component level.

Results

Figure 55 shows the prediction of temperature profile in the LSHR disk at the end of 65 minutes in the furnace set at super-solvus temperature. "Time at temp" is a critical element of process modeling to determine the transition region of coarse and fine grains as well as containing the grain growth. Figure 56 shows the macrostructure of the disk cross-section confirming the modeling prediction on clearly defined transition zone.

Figure 57 – 60 show the prediction of different gamma prime volume fraction and size distribution within the DMHT LSHR disk after the SuperCooler quenching. Predictions were made using PrecipiCalc™.

Measurements were not available at the time of generating this report. Hence, the prediction quality could not be proven. One major point was observed in the prediction as discussed below:

DMHT process requires the rim to be exposed to supersolvus temperature so that all γ' is dissolved in the solid solution, thus, enhancing the grain growth and eliminating the "pinning" mechanism of the grain boundaries. With this condition, there shall not be any primary γ' in the rim area at the end of quenching.

However, PrecipiCalc is predicting the presence of primary γ' in the rim area. Although minimal in volume fraction, fundamentally all primary γ' should have been dissolved in the rim area as it reaches the super-solvus temperature.

Summary

The predictive tools developed and used in this project could enhance the development, qualification and insertion of new materials in an engine. However, great amount of data is needed to validate the predictability of such tools as demonstrated in this study. ATI Ladish strongly recommends performing the measurement on the LSHR disk to correlate the predictions from this study.
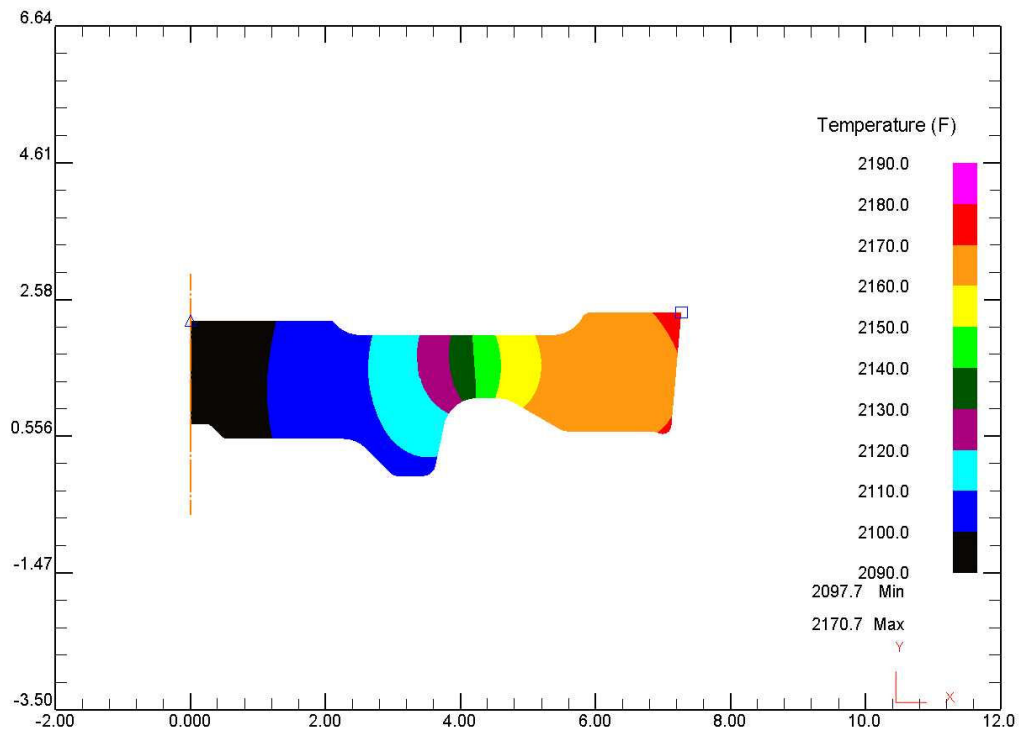
Figure 55   Temperature (F) prediction at the end of 65 minutes in the furnace set at 2175°F
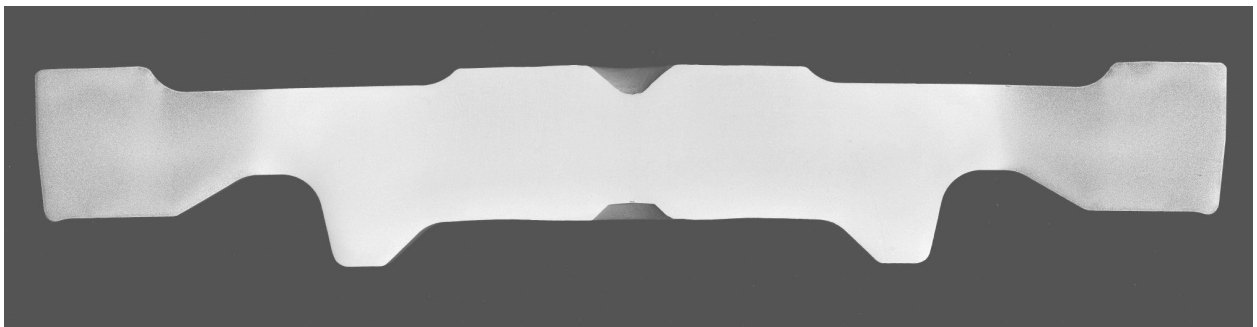[1].

Figure 56   Full radial macrostructure [1].
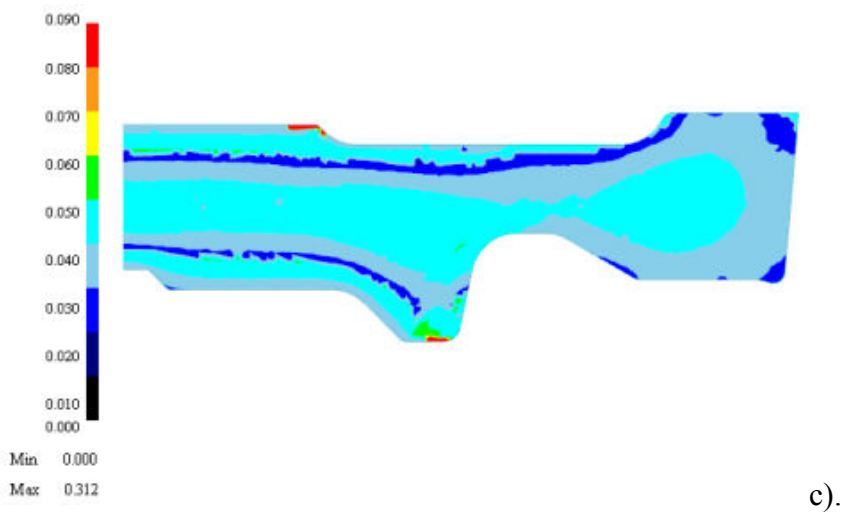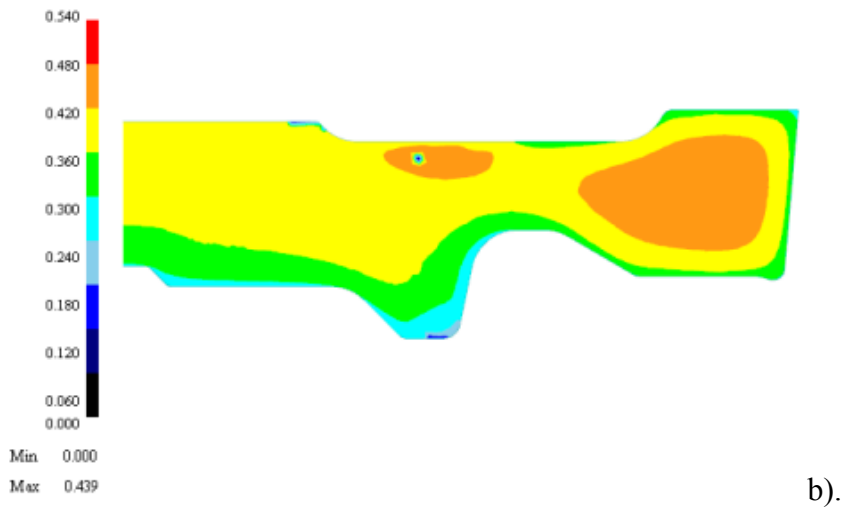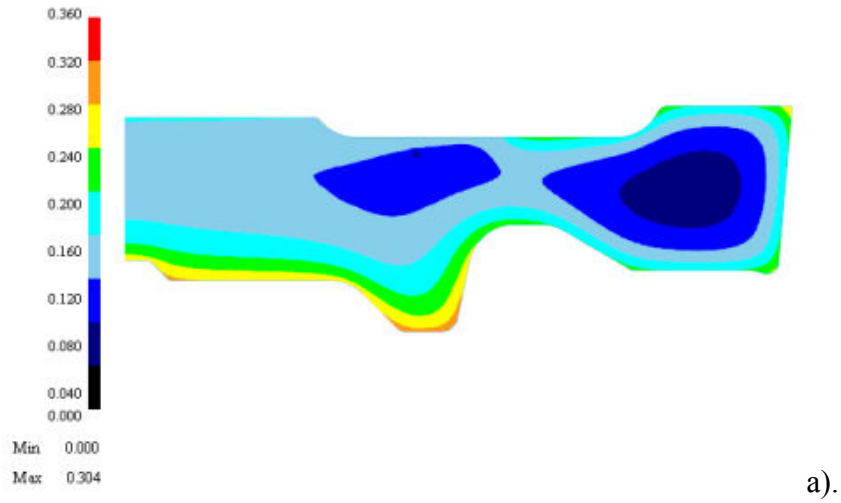
a).

b).

c).

Figure 57   Gamma prime volume fraction in the DMHT LSHR disk; a). Primary, b). Secondary, c). Tertiary.
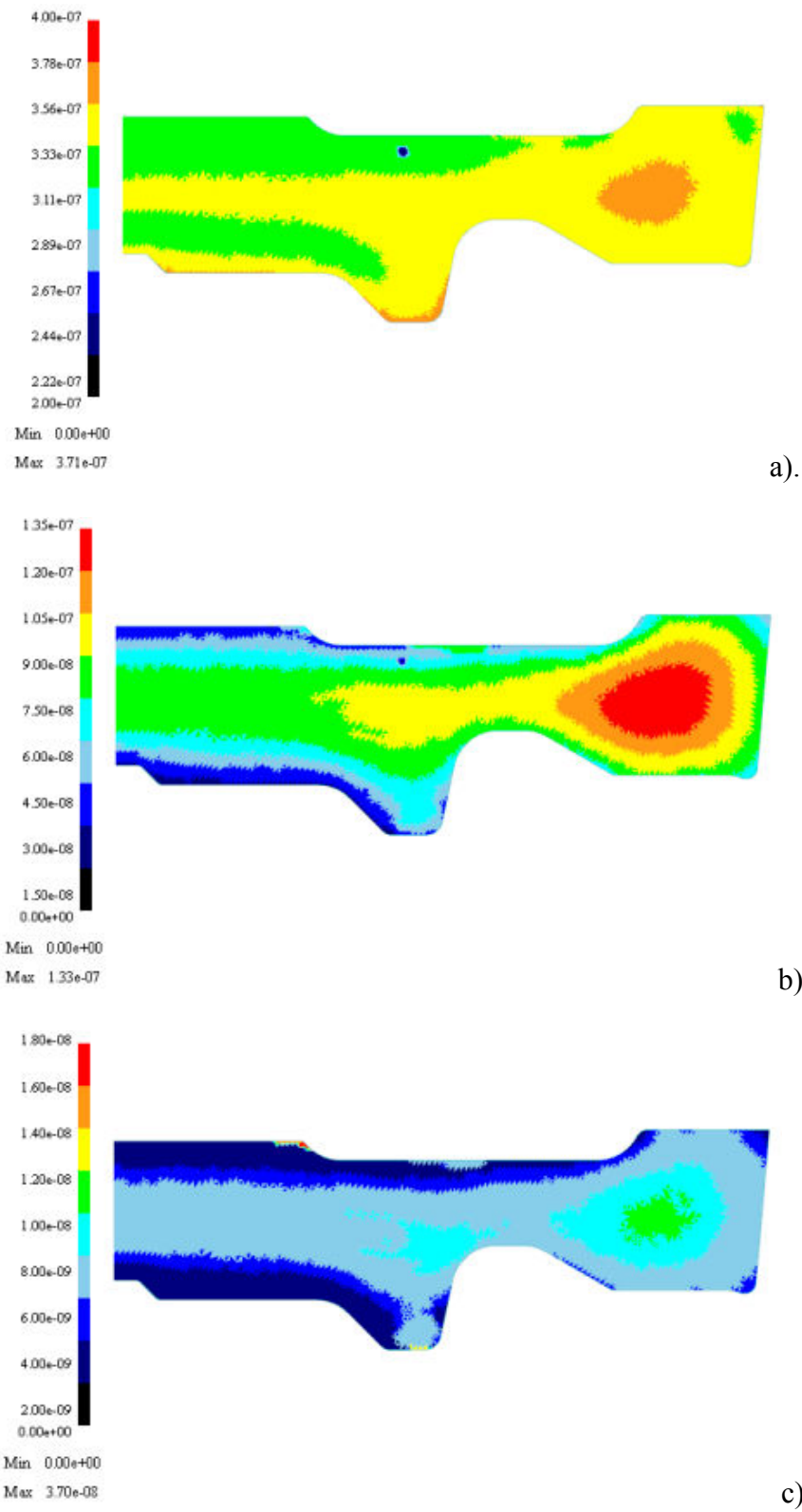
a).

b).

c).

Figure 58   Gamma prime size (in meters) in the DMHT LSHR disk; a). Primary, b).
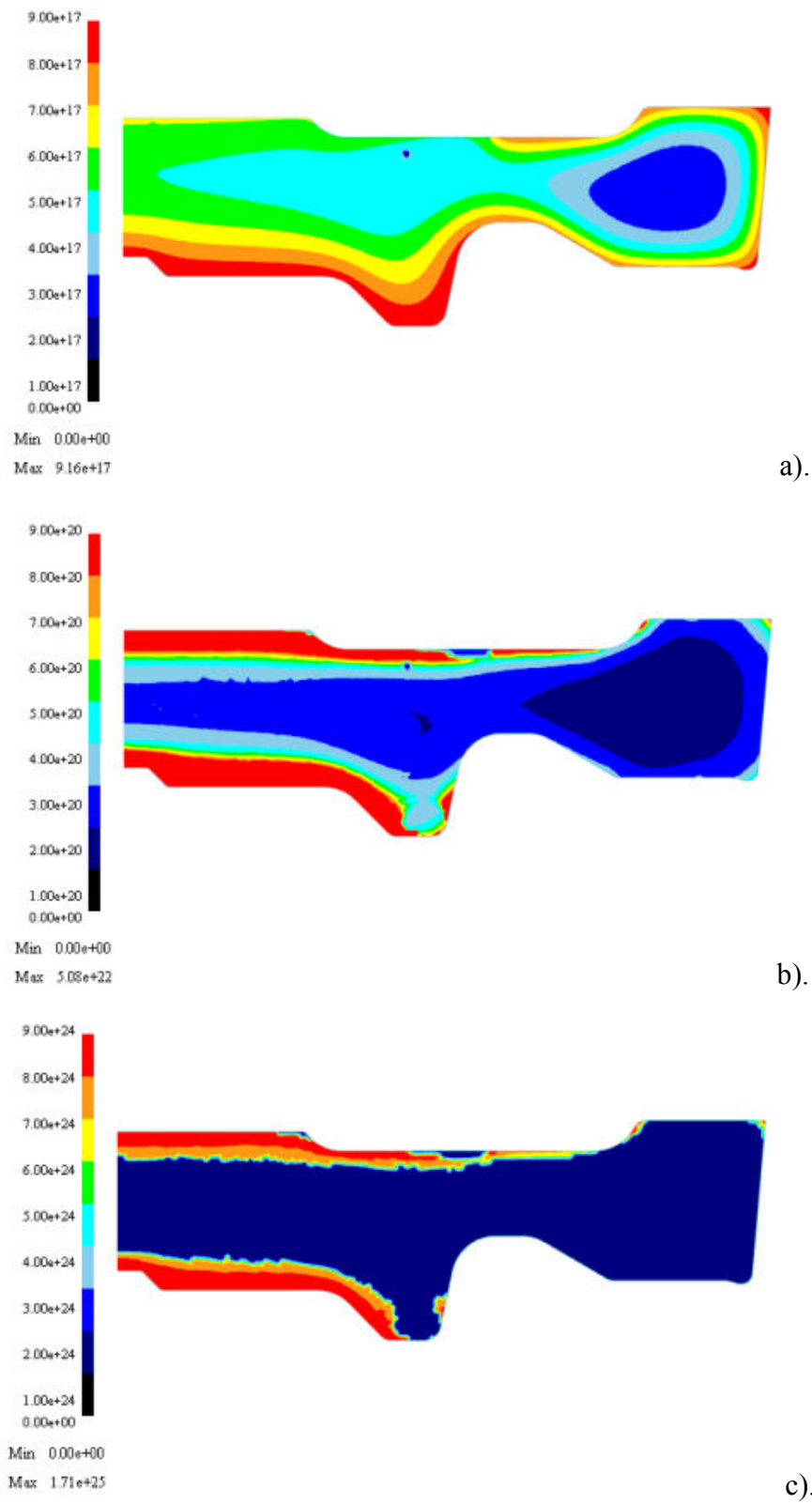   Secondary, c). Tertiary.

Figure 59   Gamma prime density (number of particles in a given area) in the DMHT LSHR disk; a). Primary, b). Secondary, c). Tertiary.
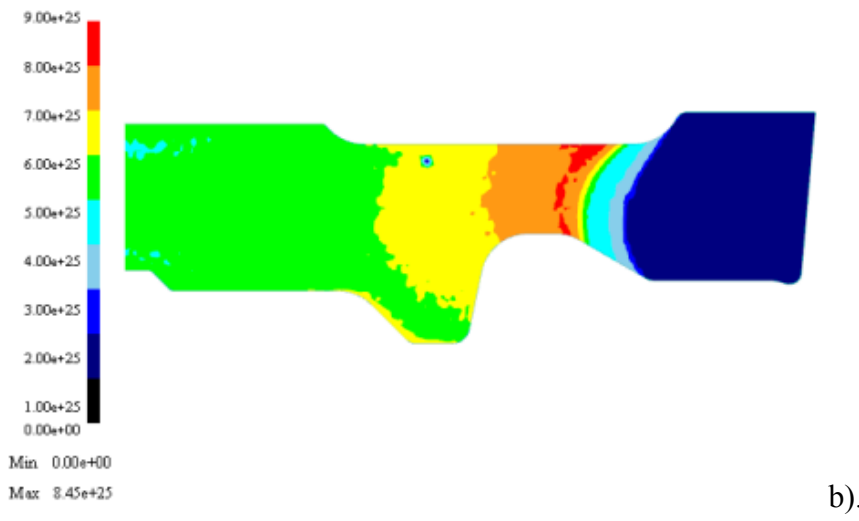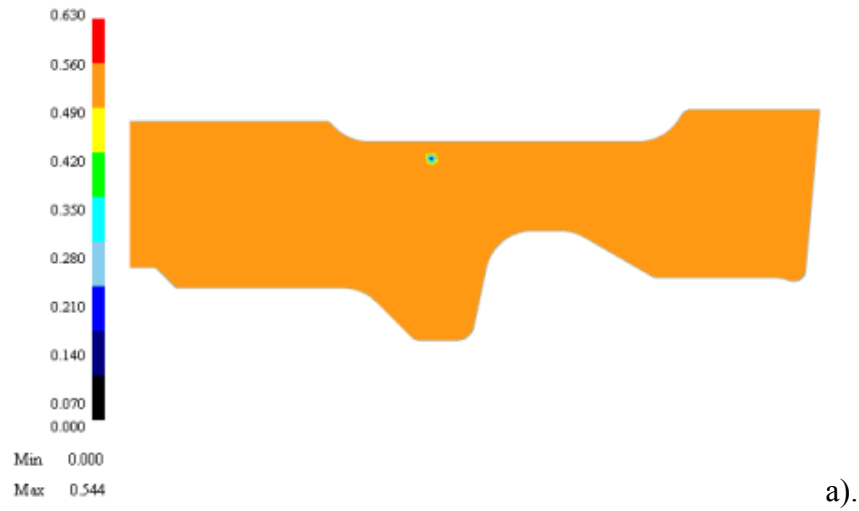
a).

b).

Figure 60   a). Total Gamma prime volume fraction; b). Total Gamma prime density
(number of particles in a given area) in the DMHT LSHR disk.

3.0 CONCLUSIONS

- The commercial FEM code DEFORM has been augmented to capture the local evolution of multiple different families of precipitates in multiphase superalloys such as LSHR.

- The presence or absence of these precipitates also affect the local grain size. Grain growth or recrystallization are impeded by the presence of precipitates via the Zener pinning phenomenon, and unimpeded when these precipitates are absent (such as during supersolvus processing).

- The local variation of precipitates and grain size established from the two previous enhancements now also influence properties. During this program, DEFORM was enhanced to include microstructure (precipitates, grain size) in the flow stress and in the creep property models. This enhancement is performed either via an empirical look-up-table, or by phenomenological physics-based models (such as Tresa Pollocks' strength model, as adapted by Northwestern University; or via the Langdon or the Dorn creep models).

- It was demonstrated during this program that the integrated location-specific grain size and precipitate size microstructure models discussed above can predict the location-specific property variation across a dual-microstructure-heat-treated (DMHT) disk.

- The variation in these properties impact the component wide performance - residual stress distribution during heat up and DMHT processing; disk distortion during machining; and disk performance (elastic distortion, plastic distortion, creep) during virtual spin-pit testing

- Ladish Corporation performed simulations on this newly integrated system, and observed that **"the predictive tools developed and used in this project could enhance the development, qualification and insertion of new materials in an engine."**

- As a result of these integrated enhancements, the DEFORM FEM code is improved in such a way as to be a valuable simulation and design tool for industrial users

REFERENCES

1   NASA/CR 2005-213574 report

2   "Modeling microstructure development in the forging of waspaloy turbine engine
        disks", Shen, 1994

3   "Thermal and Mechanical Property Characterization of the Advanced Disk Alloy
        LSHR"; NASA/CR - 213645

4   Tensile and Creep Property Characterization of Potential Brayton Cycle Impeller
        and Duct Materials" (NASA/TM-2006-204110; Gabb, T; Gayda, J

5   Tresa Pollock; Sammy Tin; "Nickel-Based Superalloys for Advanced Turbine
        Engines: Chemistry, Microstructure, and Properties", Journal of Propulsion and
        Power, v. 22, no. 2, 2006.

6   R. Prasannavenkatesan, J. Zhang, D. L. McDowell, G. B. Olson, H-J. Jou, "3D
        modeling of subsurface fatigue crack nucleation potency of primary inclusions in
        heat treated and shot peened martensitic gear steels," *International Journal of
        Fatigue,* Vol. 31, No. 7, (2009), 1176–1189.

7   J. Lemsky, ATI Ladish Forging; Dual Microstructure Heat Treated LSHR Disk
        Forgings Utilizing Ladish SuperCooler Cooling Technology; Air Force Contract:
        FA8601-08-P-0291.

8   "5 Decades of the Zener Equation", Manohar et al, ISIJ International, V. 38, no.
        9,1998.

9   Raj, S.; T, Langdon. "Creep behavior of copper at intermediate temperatures -
        mechanical   properties." Acta. Metall. v.37, no.3,1998.

10   Kassner. "Recent developments in understanding the mechanism of 5-power-law
        creep." Mat. Sci. Engr. A, v. 20-23, 2005